

2 Quantifying NO_x emissions in Egypt using TROPOMI observations

3 Anthony Rey-Pommier¹, Frédéric Chevallier¹, Philippe Ciais¹, Grégoire Broquet¹, Theodoros
4 Christoudias², Jonilda Kushta², Didier Hauglustaine¹ and Jean Sciare².

5 ¹ Laboratoire des Sciences du Climat et de l'Environnement, LSCE/IPSL, CEA-CNRS-UVSQ, Université Paris-Saclay,
6 91190 Gif-sur-Yvette, France

7 ² The Cyprus Institute, Climate and Atmosphere Research Center, 2121 Nicosia, Cyprus

8 **Correspondence:** Anthony Rey-Pommier (anthony.rey-pommier@lsce.ipsl.fr)

9 **Abstract.** Urban areas and industrial facilities, which concentrate the majority of human activity and industrial
10 production, are major sources of air pollutants, with serious implications for human health and global climate. For
11 most of these pollutants, emission inventories are often highly uncertain, especially in developing countries. Spaceborne
12 measurements from the TROPOMI instrument, onboard the Sentinel-5 Precursor satellite, are used to retrieve nitrogen
13 dioxide (NO_2) column densities at high spatial resolution. Here, we use two years of TROPOMI retrievals to map
14 nitrogen oxides ($\text{NO}_x = \text{NO} + \text{NO}_2$) emissions in Egypt with a top-down approach using the continuity equation in
15 steady state. Emissions are expressed as the sum of a transport term and a sink term representing the three-body
16 reaction comprising NO_2 and hydroxyl radical (OH). This sink term requires information on the lifetime of NO_2 ,
17 which is calculated with the use of the CAMS near-real-time temperature and OH concentration fields. We compare
18 this derived lifetime with the lifetime inferred from the fitting of NO_2 line density profiles in large plumes with an
19 exponentially modified Gaussian function. This comparison, which is conducted for different samples of NO_2 patterns
20 above the city of Riyadh, provides information on the reliability of the CAMS near-real-time OH concentration fields;
21 it also provides the location of the most appropriate vertical level to represent typical pollution sources in industrial
22 areas and megacities in the Middle East region. In Egypt, total emissions of NO_x are dominated by the sink term, but
23 they can be locally dominated by wind transport, especially along the Nile where human activities are concentrated.
24 Megacities and industrial regions clearly appear as the largest sources of NO_x emissions in the country. Our top-down
25 model infers emissions with a marked annual variability. By looking at the spatial distribution of emissions at the scale
26 of different cities with different industrial characteristics, it appears that this variability is consistent with national
27 electricity consumption. We detect lower emissions on Fridays, which are inherent to the social norm of the country,
28 and quantify the drop in emissions in 2020 due to the COVID-19 pandemic. Overall, our estimations of NO_x emissions
29 for Egypt are 7.0% higher than the CAMS-GLOB-ANT_v4.2 inventory, and significantly differ in terms of seasonality.

30

31 1 Introduction

32 Economic growth in developing countries has led to a strong increase of urban air pollution (Baklanov et al., 2016 [1]).
33 Among the different pollutants, nitrogen oxides are key species. They are generally the products of fuel combustion,
34 such as the burning of hydrocarbons in the air at high temperature. The main sources of these compounds are vehicle
35 engines, but also heavy industrial facilities such as power plants, iron and steel mills (Tang et al., 2020 [2]) and cement
36 kilns (Kim et al., 2020 [3]). Their accumulation in the lowest layers of the troposphere contributes to the formation
37 of smog and acid rain (Singh et al., 2007 [4]). They also have a significant effect on human health, as they can cause
38 various respiratory diseases (EPA, US., 2016 [5]). To deal with these phenomena, national and regional governments
39 generally enact a series of air pollution control strategies, which typically take the form of bans on certain polluting
40 technologies, with the aim of reducing the concentration of pollutants at the local level to targets that must be achieved
41 within a given timeframe. These strategies, which also help driving technological innovation, have had a significant
42 effect in Europe (Crippa et al., 2016 [6]).

43 In Egypt, population growth, urbanisation, socio-economic development and the associated increase in the vehicle

44 fleet led to a major degradation of air quality in the last decades, especially in highly populated areas such as Greater
45 Cairo and the Nile Delta (Abou El-Magd et al., 2020 [7]) which gather the majority of the population. The Ministry of
46 State for the Environment has thus initiated new policies that aim to reduce pollution levels throughout the country,
47 through technical mitigation of emissions, emission standards for vehicles and intersectoral collaboration (UNEP, 2015
48 [8]). However, Egypt, like most developing countries, lacks the local infrastructure to access detailed information on
49 technical factors such as energy consumption or fuel type and technology, leading to discrepancies in inventories (Xue
50 et al., 2012 [9]). As a consequence, the monitoring of emissions, which is important to evaluate the effects of air
51 pollution control policies, is of limited reliability.

52 To overcome the uncertainties in the emission inventories, the use of independent observations systems is becoming
53 increasingly prevalent. In this study, we investigate the use of satellite remote sensing of atmospheric concentrations to
54 improve the quantification of NO_x emissions in Egypt. Spectrally resolved satellite measurements of solar backscattered
55 radiation enable the quantification of NO_2 and other trace gases absorbing in the UV-Visible spectral range based
56 on their characteristic spectral absorption patterns. Tropospheric vertical column densities, i.e. vertically integrated
57 NO_2 concentrations in the troposphere, have been providing information on the spatial distribution of tropospheric
58 NO_2 at global scale for nearly 30 years, allowing the identification of different sources of NO_x and the quantification
59 of the associated emissions (Leue et al., 2001 [10]; Martin et al., 2003 [11]; Mijling and van der A, 2012 [12]; de Foy et
60 al., 2015 [13]; Goldberg et al., 2019 [14]; Beirle et al., 2019 [15]; Lorente et al., 2019 [16]; Lange et al., 2021 [17]). In
61 October 2017, the Sentinel-5 Precursor satellite was launched. Its main instrument is the TROPOspheric Monitoring
62 Instrument (TROPOMI), which provides tropospheric NO_2 column densities at high spatial resolution with a large
63 swath width and with a daily frequency (Veeckind et al., 2012 [18]). By applying the steady-state continuity equation
64 (Beirle et al., 2019 [15]; Lama et al., [19], 2020), it is possible to build a top-down model that directly quantifies NO_x
65 emissions from these NO_2 column densities, provided that some key parameters (wind, temperature, hydroxyl radical
66 concentration and concentration ratio between NO_x and NO_2) are correctly estimated. This model is used to quantify
67 the anthropogenic NO_x emissions in Egypt for a 2-year period, from November 2018 to November 2020.

68 This paper is organised as follows: Section 2 provides a description of the datasets used in this study. Section
69 3 explains the build-up and the limits of the top-down approach used to quantify NO_x emissions in Egypt. It also
70 presents a method for validating the model parameters by using NO_2 line density profiles over Riyadh, Saudi Arabia.
71 Section 4 presents the analysis of this validation method. It presents the location of the main NO_x sources in Egypt
72 and evaluates the vertical sensitivity of the model. It also assesses the ability of the model to show less human activity
73 on Fridays and during the lockdown that took place during the COVID-19 pandemic. It finally confronts the inferred
74 emissions with different inventories in terms of amplitude and seasonality. Section 5 presents our conclusion and
75 general remarks.

76 2 Instrumentation and data

77 2.1 TROPOMI NO_2 retrievals

78 The TROPOspheric Atmosphere Monitoring Instrument (TROPOMI), onboard the European Space Agency’s (ESA)
79 Sentinel-5 Precursor (S-5P) satellite, provides measurements for atmospheric composition. TROPOMI is a spectrom-
80 eter observing wavelengths in the infrared, visible and ultraviolet light at around 13:30 local time. The UV-Visible
81 spectral band at 405-465 nm is used to retrieve NO_2 . Other spectral bands are used to observe methane, formalde-
82 hyde, sulphur dioxide, carbon monoxide and ozone, as well as aerosols and cloud physical properties. The very high
83 spatial resolution offered by TROPOMI (originally $3.5 \times 7 \text{ km}^2$ at nadir, improved to $3.5 \times 5.5 \text{ km}^2$ since 6 August
84 2019) provides unprecedented information on tropospheric NO_2 . Its large swath width ($\sim 2600 \text{ km}$) makes it possible
85 to construct NO_2 images on large spatial scales. Those images greatly improve the potential for detecting highly
86 localised pollution plumes above the ground, identifying small-scale emission sources but also estimating emissions
87 from megacities, industrial facilities and biomass burning. We use TROPOMI NO_2 retrievals (Level 2 data, OFFL
88 stream) from November 2018 to November 2020 over Egypt. We also use them over Saudi Arabia, and more specifi-
89 cally over the city of Riyadh, to evaluate the reliability of other parameters. This will be explained in Section 3.3.
90 Both countries have an arid climate, which offers a large number of clear-sky days throughout the year, enabling the
91 calculation of monthly averages based on more than 20 observations. They are also the host to many large plumes of
92 pollutants due to high human concentrations along rivers and around megacities, which allows us to observe high NO_2
93 concentration patterns with a high signal-to-noise ratio. TROPOMI products provide a quality assurance value q_a ,
94 which ranges from 0 (no data) to 1 (high-quality data). For our analysis of concentrations, we selected NO_2 retrievals
95 with q_a values greater than 0.75, which systematically correspond to clear-sky conditions (Eskes et al., 2019 [20]).

96 TROPOMI soundings are gridded at a spatial resolution of $0.1^\circ \times 0.1^\circ$ with daily coverage. This resolution is lower
97 than that of the instrument; the gridding thus provides a grid for which most NO_2 columns correspond to one or more
98 measurements. The observed plumes remain correctly resolved. Cells without measurements are infrequent, which
99 facilitates the calculation of derivatives.

100 2.2 Wind data

101 The horizontal wind $\mathbf{w} = (u, v)$ is taken from the European Centre for Medium-Range Weather Forecasts (ECMWF)
102 ERA5 data archive (fifth generation of atmospheric reanalyses) at a horizontal resolution of $0.25^\circ \times 0.25^\circ$ on 37
103 pressure levels (Hersbach et al., 2020 [21]). The hourly values have been linearly interpolated to the TROPOMI orbit
104 timestamp and re-gridded to a $0.1^\circ \times 0.1^\circ$ resolution.

105 2.3 CAMS real-time fields

106 The Copernicus Atmospheric Monitoring Service (CAMS) global near-real-time service provides analyses and forecasts
107 for reactive gases, greenhouse gases and aerosols on 25 pressure levels with a horizontal resolution of $0.4^\circ \times 0.4^\circ$ and
108 a temporal resolution of 3 hours (Huijnen et al., 2016 [22]). For the calculation of NO_x emissions from TROPOMI
109 observations, we use CAMS concentration fields of nitrogen oxides (NO and NO_2) and hydroxyl radical (OH). We
110 also use the CAMS temperature field T . NO and NO_2 concentrations are used to account for chemical processes that
111 take place in polluted air. Anthropogenic activities produce mainly NO , which is transformed into NO_2 by reaction
112 with ozone O_3 . NO_2 is then photolyzed during the day, reforming NO (Seinfeld, 1989 [23]). This photochemical
113 equilibrium between NO and NO_2 can be highlighted with the $\text{NO}_x:\text{NO}_2$ concentration ratio, whose value depends on
114 local conditions, allowing to perform a conversion from NO_2 production to NO_x emissions. The reason for the use of
115 OH is different. OH is the main oxidant that controls the ability of the atmosphere to remove pollutants such as NO_2
116 (Logan et al., 1981 [24]). It is mainly produced during daylight hours by interaction between water and atomic oxygen
117 produced by ozone dissociation (Levy, 1971 [25]). In air that is directly influenced by pollution, another source of OH
118 is due to a reaction between NO and HO_2 . This reaction, referred to as the NO_x recycling mechanism, illustrates the
119 nonlinear dependence of the OH concentration on NO_2 (Valin et al., 2011 [26]; Lelieveld et al., 2016 [27]). Since the
120 OH lifetime is typically of less than a second, its concentration in the troposphere is very low and difficult to measure.
121 As a consequence, global analyses, which estimate OH concentrations from other variable species (Li et al., 2018 [28];
122 Wolfe et al., 2019 [29]), provide a representation for OH concentrations with high associated uncertainties. Therefore,
123 the CAMS OH concentrations are used here to account for the NO_2 oxidation to form nitric acid (HNO_3), whose
124 representation is explained in Section 3.1. Finally, the temperature field is used to control variations in the kinetic
125 parameters (Burkholder et al., 2020 [30]). The hourly values are also linearly interpolated to the TROPOMI orbit
126 timestamp and re-gridded to a $0.1^\circ \times 0.1^\circ$ resolution.

127 2.4 Background removal

128 Detecting traces of anthropogenic emissions in TROPOMI NO_2 images is not a straightforward process. The NO_2
129 signal from a sparsely populated area or a small industrial facility may be covered by numerical noise or by the signal
130 generated by natural NO_x emissions. In the absence of anthropogenic sources, TROPOMI observes NO_2 concentrations
131 which constitute a tropospheric background of $\sim 0.5 \times 10^{15}$ molecules. cm^{-2} . At the global scale, this background is the
132 result of different sources. In the lower troposphere, natural NO_x emissions are mostly due to fires and soil emissions
133 (Yienger et al., 1995 [31], Hoelzemann et al., 2004 [32]). In the upper troposphere however, sources include lightning,
134 convective injection and downwelling from the stratosphere (Ehhalt et al., 1992 [33]), but the factors controlling the
135 resulting concentrations are poorly understood. According to state-of-art estimates, anthropogenic NO_x accounts for
136 most of the emissions at the global scale, whereas natural emissions from fires, soils and lightning are less significant at
137 the global scale and do not exceed a share of 35% combined (Jaeglé et al., 2005 [34]; Müller and Stavrou, 2005 [35]),
138 although associated errors can be very high. In eastern China, the non-anthropogenic share of total NO_x emissions is
139 variable but does not exceed 20% (Lin, 2012 [36]). Egypt being a desertic region and not very conducive to lightning,
140 we expect the share of those non-anthropogenic emissions to be smaller. To estimate anthropogenic NO_x emissions,
141 it is therefore necessary to remove this share.

142 With an atmospheric lifetime of about a few hours, the presence of NO_2 is relatively short. Consequently, the
143 majority of NO_2 is not transported far downwind from its sources. Thus, near-surface NO_2 concentrations are generally
144 high over industrial facilities and densely populated areas that need to be identified. Because Egypt's population is
145 almost entirely located along the Nile River and its delta, the study of NO_x emissions in this country cannot therefore
146 be reduced to the study of a small number of point sources, as it would be the case for several other parts of the

147 Middle East region, and must be carried out in the form of a mapping of the country. Further discussion is provided
 148 in Section 3.3. To identify urban areas in Egypt, we use the Socioeconomic Data and Applications Center (SEDAC)
 149 GRUMP (Global Rural-Urban Mapping Project) data archive, which comprises eight global datasets, including a
 150 population density grid provided at a resolution of 30 arc seconds, with population estimates normalised for the year
 151 2000 (CIESIN, 2019 [37]). We combine this database with field data giving the location of industrial facilities from
 152 energy-intensive industries in the region (data have been retrieved from the Global Energy Observatory for oil and
 153 gas-fired power plants, from IndustryAbout for aluminium and iron smelters, from the work of Elvidge et al., 2016
 154 [38] for flaring sites, and from the work of Steven J. Davis and Dan Tong for cement plants; links at the end of this
 155 article).

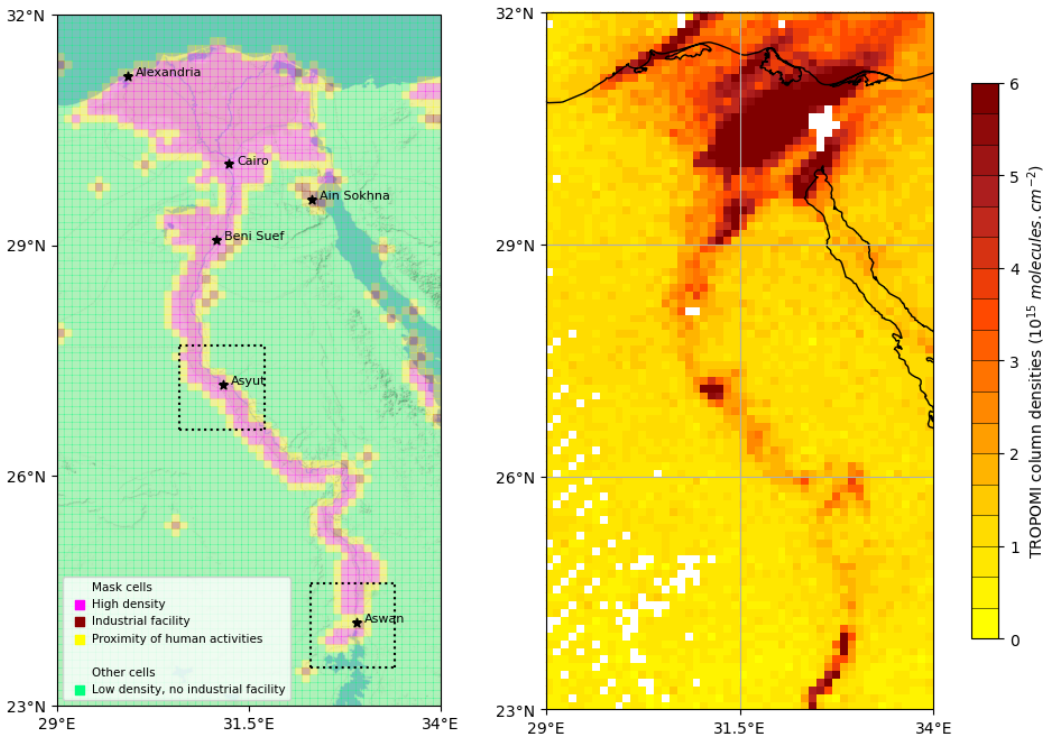


Figure 1: (left) Part of Egypt centered on Nile River. Within this domain, pink cells represent locations with an average human density above 100 hab.km^{-2} , brown cells represent locations with industrial facilities outside cities, and yellow cells represent locations in their vicinity. These cells constitute the mask used to calculate anthropogenic emissions. Outside this mask, green cells represent areas which do not correspond to any of the three criteria, considered to be void of human activity. Five largest cities in the country and the industrial area of Ain Sokhna are denoted with stars. Two smaller domains centered around the cities of Asyut and Aswan are represented with dotted lines; their use is presented in Section 4.6. (right) TROPOMI observation of NO_2 slant column densities above Nile valley on 3 January 2019. White pixels correspond to areas with low quality data ($q_a < 0.75$) or no data.

156 These datasets are used to remove the non-anthropogenic part of the NO_x emissions signal. We conduct this removal
 157 by subtracting the mean emissions over areas without human activity from the mean emissions over industrial and
 158 densely populated areas. In order to perform this distinction between these two types of areas, our study is carried
 159 out using a mask within a $0.1^\circ \times 0.1^\circ$ grid. A grid cell is considered to be part of the mask if it has a population
 160 density higher than a threshold of 100 hab.km^{-2} , or if its centre is close to an industrial facility. Otherwise, the
 161 cell is considered to be part of the "background", i.e. outside the mask. In order to avoid any smearing that would
 162 correspond to abnormally high emissions outside urban and industrial centres (which can happen if the wind is poorly
 163 estimated), transition cells (in the immediate vicinity of the mentioned mask cells) are also considered to be mask
 164 cells. Figure 1 shows the distinction between mask cells and background cells on our domain in Egypt that lies
 165 between parallels 23°N and 32°N and meridians 29°E and 34°E . Most of the mask cells are located in the Nile area.
 166 Some mask cells are also found on the coast or in isolated parts in the desert. They correspond to remote industrial
 167 facilities, including major flaring sites, or sparsely populated industrial centres such as Ain Sokhna's industrial area.
 168 The domain comprises $n_m = 949$ mask cells and $n_b = 3692$ background cells. The mathematical description of the
 169 background removal is outlined in Section 3.4.

170 2.5 Emission inventories

171 We compare TROPOMI-derived NO_x emissions to the Emissions Database for Global Atmospheric Research
172 (EDGARv5.0) for 2020 and the CAMS global anthropogenic emissions (CAMS-GLOB-ANT_v4.2) inventory released
173 in 2020. Both datasets provide $0.1^\circ \times 0.1^\circ$ gridded emissions for different sectors on a monthly basis. EDGARv5.0
174 emissions are based on activity data (population, energy production, fossil fuel extraction, industrial processes, agricul-
175 tural statistics, etc.) derived from the International Energy Agency (IEA) and the Food and Agriculture Organization
176 (FAO), corresponding emission factors, national and regional information on technology mix data and end-of-pipe
177 measurements. The inventory covers the years 1970-2015 and differs from the previous version EDGARv4.3.2 which
178 does not use splitting factors derived from the Energy Information Administration (EIA) data on fuel consumption of
179 coal, oil and natural gas for specific countries (Crippa et al., 2020 [39]). CAMS-GLOB-ANT_v4.2 is developed within
180 the framework of the Copernicus Atmospheric Monitoring Service (Granier et al., 2019 [40]). For this inventory, NO_x
181 emissions are based on various existing sectors in the EDGARv4.3.2 emissions from 2000-2012 which are used as a basis
182 for 2010 emissions and are extrapolated to the current year using 2011-2014 sector-based trends from the Community
183 Emissions Data System (CEDS) inventory (Hoesly et al., 2018 [41]). From one inventory to another, the names and
184 definitions of the sectors may vary. In EDGARv5.0 and CAMS-GLOB-ANT_v4.2, the emissions for a given country
185 are derived from the type of technologies used, the dependence of emission factors on fuel type, combustion conditions,
186 as well as activity data and low resolution emission factors (Janssens-Maenhout et al., 2019 [42]).

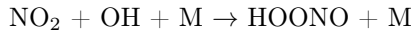
187 3 Method

188 3.1 Calculation of NO_2 production from TROPOMI observations

189 As a first step, we use tropospheric NO_2 vertical column densities Ω_{NO_2} to derive top-down NO_2 production maps.
190 Vertical column densities Ω_{NO_2} are obtained from TROPOMI slant column densities using an air mass factor (AMF)
191 which is also provided by TROPOMI. Previous studies have shown that the use of the AMF is a source of structural
192 uncertainty in NO_2 retrievals (Boersma et al., 2004 [43]; Lorente et al., 2017 [44]). In polluted environments, this
193 source of uncertainty becomes non-negligible. Here, the AMF does not vary much temporally throughout the studied
194 period, and is around 1.6 for mask cells and around 1.9 for background cells. The difference between the two types of
195 cells is probably due to a different albedo between the urban environment and desert areas. Using the horizontal wind
196 \mathbf{w} , the NO_2 flux is given as $\Omega_{\text{NO}_2} \mathbf{w}$. The divergence of this flux can be added to the local time derivative $\frac{\partial \Omega_{\text{NO}_2}}{\partial t}$ to
197 balance NO_2 sources e_{NO_2} and sinks s_{NO_2} according to the continuity equation:

$$\frac{\partial \Omega_{\text{NO}_2}}{\partial t} + \text{div}(\Omega_{\text{NO}_2} \mathbf{w}) = e_{\text{NO}_2} - s_{\text{NO}_2} \quad (1)$$

198 In steady state, the time derivative disappears and the mass balance is reduced to three terms. The NO_2 production
199 can thus be estimated by taking the combined effect of atmospheric transport losses and the different sinks. For the
200 transport term, we calculate numerical derivatives with a fourth-order central-finite difference scheme for each cell of
201 the domain. Moreover, since the local overpass time of TROPOMI occurs is in the middle of the day, NO_2 losses are
202 largely dominated by the three-body reaction involving NO_2 and OH (Seinfeld, 1989 [23]). Two channels have been
203 identified for this reaction (Burkholder et al., 2020 [30]), leading to the production of nitric acid HNO_3 and pernitrous
204 acid HOONO:



207 For the OH concentrations that are considered in this region ($1\text{-}20 \times 10^6$ molecules. cm^{-3}), the reactions above follow
208 first order kinetics. The total sink term can therefore be calculated as $s_{\text{NO}_2} = \Omega_{\text{NO}_2} / \tau$ with:

$$\tau = \frac{1}{k_{\text{mean}}(T, [\text{M}]) \cdot [\text{OH}]} \quad (2)$$

209 τ appears here as the characteristic mixed lifetime of NO_2 in the atmosphere. The reaction rate k_{mean} characterises
210 the reactions between NO_2 and OH and depends on atmospheric conditions. Burkholder et al., 2020 [30] provide a
211 general expression of this rate as a function of both temperature T and total air concentration $[\text{M}]$. Note that although
212 this reaction rate accounts for both reactions with OH, the second channel is minor, because HOONO can be rapidly
213 decomposed back to NO_2 and OH in the lower troposphere. The value of k_{mean} therefore represents the total loss of
214 NO_2 due to OH, with a contribution of the HOONO forming reaction between 5 to 15% under atmospheric conditions

215 (Sander et al., 2011 [45]; Nault et al., 2016 [46]). Thus, the NO_2 production can be calculated as the sum of a transport
216 term and a sink term:

$$e_{\text{NO}_2} = \text{div}(\Omega_{\text{NO}_2} \mathbf{w}) + \Omega_{\text{NO}_2} / \tau \quad (3)$$

217 The treatment for NO_x removal is simplified here. NO_x concentrations are influenced by other sinks. Stavrou et
218 al., 2013 [47] showed that the reaction between NO_2 and OH forming HNO_3 accounted for 26 to 64% of total NO_x
219 loss at the global scale. However, the features of the climate in Egypt during daytime hinder many other processes
220 to have a significant effect. The following NO_x sinks, which can be of notable importance at the global scale, are not
221 taken into account here:

222 - NO_2 deposition through the leaf stomata of vegetation. This sink can be significant in forested areas. In Egypt,
223 the leaf area index is very low, except in the croplands of the Nile Delta where it is comparable to that of southern
224 Europe or the western United States (Fang et al., 2019 [48]), for which the corresponding lifetime was of about 10-
225 100 h (Delaria et al., 2020 [49]), i.e. about an order of magnitude larger than the lifetimes calculated here. To our
226 knowledge, there are no studies focusing on the corresponding lifetimes for croplands, and we therefore do not take
227 this sink into account.

228 - NO_x oxidation by organic radicals to produce of alkyl and multifunctional nitrates (Sobanski et al., 2017
229 [50]). This sink increases with the concentration of volatile organic compounds (VOC), whose presence cannot be
230 excluded in Egypt. Different models have estimated low biogenic isoprene emissions in the region. These emissions
231 are concentrated at the level of the Nile and its delta (Guenther et al., 2006 [51]). They are certainly noticeable and
232 higher in summer than in winter, and contrast with the rest of the country, but they remain low compared to other
233 regions in the world. They are, for instance, about an order of magnitude lower than in the forested areas of the
234 eastern US, where the corresponding sink accounts for between 30% and 60% of the total NO_x sink (Romer Present
235 et al., 2020 [52]). Furthermore, at large NO_2 concentrations (compared to VOC concentrations), the share of this sink
236 in the total NO_x loss is weakened compared to that of HNO_3 (Romer Present et al., 2020 [52]). The effect of biogenic
237 emissions of VOC can therefore be considered minor. However, VOC emissions can also be of anthropogenic origin,
238 especially in urban areas, where they are difficult to estimate. To our knowledge, there is no study evaluating the
239 competition of the two sinks in Egypt or in a region with similar features and we therefore do not account for this
240 reaction in our calculations.

241 - NO reaction with HO_2 to produce nitric acid (Butkovskaya et al., 2005 [53]), whose yield is strongly enhanced in
242 presence of water vapour (Butkovskaya et al., 2009 [54]). Here, we neglect this reaction as the corresponding reaction
243 rate is lower by a factor 3 to 8 in dry conditions (Butkovskaya et al., 2005 [53]);

244 - NO conversion to NO_3 , the latter being in thermal equilibrium with NO_2 and N_2O_5 . This sink, which takes place
245 via heterogeneous processes, has a significant contribution during nighttime in the Mediterranean region (Friedrich et
246 al., 2021 [55]), is neglected at 13:30 when OH is close to its daily maximum;

247 - NO_2 reversible reaction with peroxyacetyl radical to produce peroxyacetylnitrate (Moxim et al., 1996 [56]). In
248 the Nile Delta region, PAN concentrations in the lower troposphere are significantly below the global average (Fischer
249 et al., 2014 [57]), suggesting a small yield. Moreover, its production peaks in the late afternoon and early evening
250 (Seinfeld, 1989 [23]). We therefore do not consider this sink in the representation of NO_x emissions at 13:30;

251 - NO_2 uptake onto black carbon particles (Longfellow et al., 1999 [58]). This uptake is of limited amount in the
252 Mediterranean region (Friedrich et al., 2021 [55]).

253 All these processes not being accounted for, the reaction between NO_2 and OH is the only sink that is considered
254 in our calculations to provide an indication of NO_x emissions. Section 4.7 details the consequences of not considering
255 these various minority sinks on the results.

256 3.2 Interpolation to daily average emissions

257 All parameters are evaluated at 13:30 local time, which means that the NO_2 production is calculated at the same
258 moment. In Egypt, the maximum and minimum electricity consumption are reached around 20:00 and 6:00 local time
259 respectively, and inter-daily consumption differences have been weakened by the increasing sales of air conditioning
260 and ventilation systems in the past decades (Attia et al., 2012 [59]). The daily load profiles provided by the National
261 Egyptian Electricity Holding Company show that the mean daily electricity consumption corresponds approximately
262 to the consumption at 13:30 in the country (EEHC, 2021 [60]). The difference between the two quantities being small
263 both in summer (about +2 to -3%) and winter (about -2 to -6%), we consider our inferred emissions as representative
264 of the average activity in Egypt at any time of the year. This assumes that electricity consumption dominates
265 the emissions of the country, or that the other emitting sectors have a similar daily profile. This can be justified.
266 According to CAMS-GLOB-ANT_v4.2, the power sector accounts for 50 to 60% of total NO_x emissions in Egypt.

267 EDGARv5.0 presents a lower share (40 to 45% of total emissions). Moreover, for both inventories, the transport
 268 sector accounts for the majority of the remaining emissions. According to the traffic congestion index in Cairo
 269 (https://www.tomtom.com/en_gb/traffic-index/cairo-traffic/), the congestion level around 13:30 seems to be slightly
 270 higher than during the morning peak, but lower than the during night peak. Traffic emissions at this moment of the
 271 day could therefore be representative of the average traffic emissions as well.

272 3.3 Validation of CAMS OH concentration using line density calculations for Riyadh

273 When the transport term is integrated over large spatial scales, it cancels out due to the mass balance in the continuity
 274 equation between NO₂ sources and NO₂ sinks. At first order, the integration of the inferred emissions over the whole
 275 domain (of about 490,000 km²) thus reflects chemical losses of the sink term. In this term, the NO₂ lifetime calculation
 276 involves the reaction rate k_{mean} , whose annual variability is low due to small changes in Egyptian midday temperatures
 277 throughout the year, and OH concentration, whose annual variability is highly marked. In Egypt, tropospheric OH
 278 concentrations, which are strongly correlated with solar ultraviolet radiation (Rohrer and Berresheim, 2006 [61]) and
 279 NO_x emissions, are higher in summer than in winter. To ensure an appropriate representation of the OH field by
 280 CAMS data, we select a large number of TROPOMI images characterised by a homogeneous wind field, in which
 281 we calculate the NO₂ lifetime according to Equation (2), where [OH] corresponds to the near-real-time CAMS data
 282 and k_{mean} is calculated with the formula from Burkholder et al., 2020 [30]. We compare this value with the lifetime
 283 determined by a method initially developed by Beirle et al., 2011 [62], and expanded by Valin et al., 2013 [63] by
 284 introducing a rotation of the image to refine the chemical lifetime. This method consists in fitting an exponentially
 285 modified Gaussian function (EMG) to NO₂ line density profiles. These profiles correspond to the integrated NO₂
 286 columns along the mean wind direction in the pollution pattern and centered around the source. They are obtained
 287 by rotating TROPOMI images in the mean wind direction and using the values of the nearest columns in a 100 km²
 288 area. Line density profiles are generated on a span of 300 km. An example is given in Figure 3. Within the average
 289 profile, the NO₂ burden and lifetime can be derived from the parameters that describe the best statistical fit. The
 290 EMG model is expressed as follows (Lange et al., 2021 [17]):

$$\langle \Omega_{\text{NO}_2} \rangle(x|B, A, x_0, \mu, \sigma) = B + \frac{A}{2x_0} \exp\left(\frac{\mu - x}{x_0} + \frac{\sigma^2}{2x_0^2}\right) \operatorname{erfc}\left(-\frac{1}{\sqrt{2}}\left(\frac{x - \mu}{\sigma} - \frac{\sigma}{x_0}\right)\right) \quad (4)$$

291 Here, x is the distance in the downwind-upwind direction, B is the NO₂ background, A is the total number of
 292 NO₂ molecules observed in the vicinity of the point source, x_0 is the e-folding distance downwind, representing the
 293 exponential length scale of NO₂ decay, μ is the location of the apparent source relative to the centre of the point
 294 source, and σ is the standard deviation of the Gaussian function, representing the length scale of Gaussian smoothing.
 295 Using a non-linear least squares fit, we estimate the five unknown parameters: A , B , x_0 , μ and σ . From the mean
 296 wind module w_{mean} in the domain, the mean effective NO₂ lifetime τ_{fit} can be estimated using the fitted parameters:

$$\tau_{\text{fit}} = \frac{x_0}{w_{\text{mean}}} \quad (5)$$

297 The geography of Egypt does not suit the method described here. The Egyptian population is contiguously concen-
 298 trated along the Nile, which makes it difficult to define point sources isolated from human activity. Furthermore,
 299 large isolated cities such as Alexandria or Suez are too close to the coast for the wind to be considered homoge-
 300 neous. We therefore use the city of Riyadh, Saudi Arabia (24.684°N, 46.720°E) to perform the comparison between
 301 the CAMS-induced lifetime and the fit-obtained lifetime. Riyadh has been the focus of anterior studies (Valin et al.,
 302 2013 [63], Beirle et al., 2019 [15]), and is particularly suitable for several reasons. Firstly, Riyadh is a city within the
 303 latitudinal extend of Egypt (1600 km from Cairo) with a climate which is similar to the typical Egyptian climate.
 304 Secondly, NO₂ tropospheric columns over Riyadh are high ($\sim 9 \times 10^{15}$ molecules.cm⁻²), leading to retrievals with a
 305 high signal-to-noise ratio. Thirdly, Riyadh is far from the coast, and its flat terrain makes the surrounding wind fields
 306 rather homogeneous during most of the year.

307 As the fitting algorithm is very sensitive to any disturbance that might be induced by NO₂ production from other
 308 point sources, it is necessary to identify heavy industrial facilities in the area. Riyadh is also an industrial area, with
 309 several power plants located close to the city centre. Figure 2 shows the location of the most important emitters in the
 310 region, which include five gas-fired power plants (PP7, PP8, PP9, PP10 and PP14), one oil-fired power plant (PP4)
 311 and one cement plant (CP). The five gas power plants, with a total capacity of more than 10 GW, are located in the
 312 periphery of the city. These power plants are sufficiently far away from the city centre for TROPOMI to distinguish
 313 their own emissions from those of Riyadh's centre with a resolution of $0.1^\circ \times 0.1^\circ$, which is not the case for CP and
 314 PP4 which are located in the city centre. It is therefore appropriate to restrict the study of NO₂ patterns over Riyadh

315 to days for which the emissions from the city centre and those from the gas power plants do not overlap. This is the
 316 case when the wind blows steadily and homogeneously in a north-south direction. Within about 150 km around the
 317 city centre, we thus calculate the average wind given by ERA5 and consider the observation as reliable if the mean
 318 angle (θ) of the observations deviates by less than 40° from the north or the south, with a standard deviation σ_θ of less
 319 than 36° . This condition generally leads to a selection of observations with large wind speeds, low winds speeds being
 320 often associated with more variable directions. This ensures the NO_2 decay to be dominated by chemical removal and
 321 not by the variability of the wind (Valin et al., 2013 [63]). Finally, we select observations with clear-sky conditions
 322 downstream of the flow (with at least 80% downstream cells with $q_a > 0.75$).

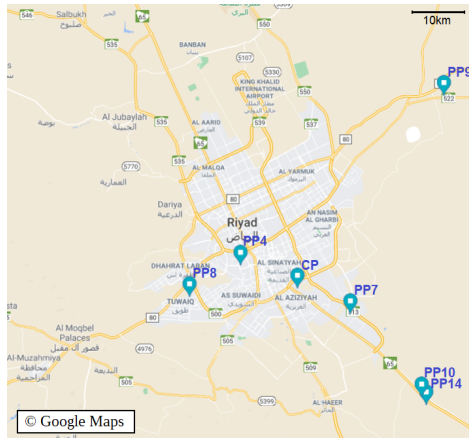


Figure 2: Map of Riyadh's city centre with the surrounding power plants (PP4, 7, 8, 9, 10 and 14) and cement plant (CP). The map has been extracted from Google Maps.

323 Our $0.1^\circ \times 0.1^\circ$ gridding ensures that retrieved lifetimes are governed by physical decay of NO_2 and not an artifact of
 324 the spatial resolution (Valin et al., 2011 [26]). The fitting procedure is very sensitive to the wind direction. Instead of
 325 manually correcting the ERA5 wind field for individual NO_2 patterns, the curve fitting is performed for every sample
 326 with three different rotation angles, corresponding to the wind direction with a correction of -10° , 0° or 10° . A record
 327 is kept if one of these three fits leads to a correlation with the corresponding NO_2 line density whose coefficient is
 328 greater than 0.97. Among the remaining samples, we keep those with a value of τ_{fit} greater than 1.0 hr (considered
 329 sufficiently high to be relevant). An example of curve fitting is given in Figure 3.

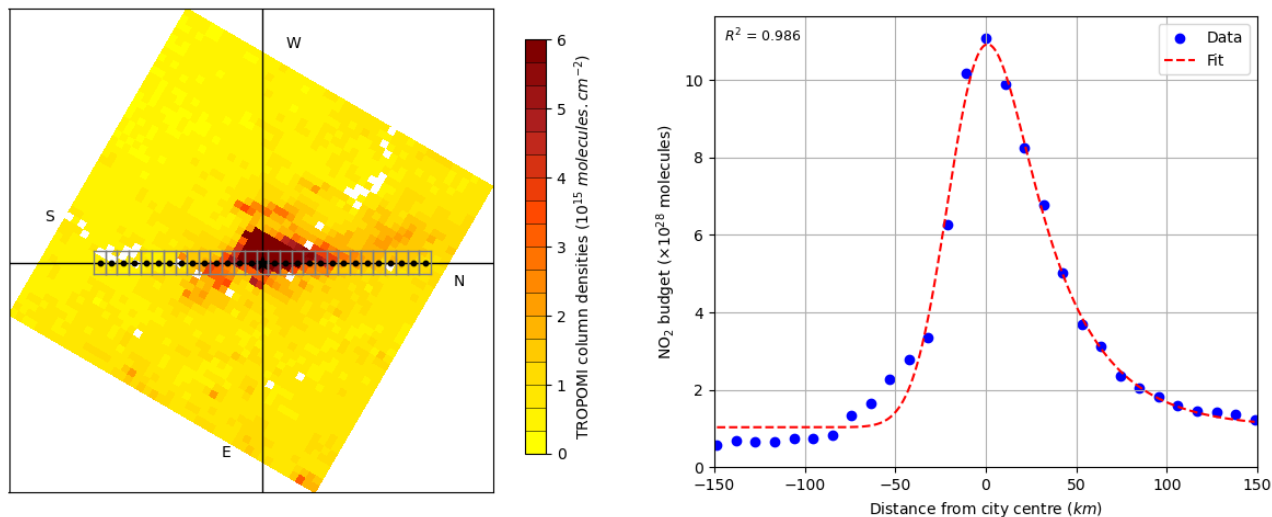


Figure 3: Estimation of the NO_2 lifetime from a pattern above Riyadh on 11 March 2020: (left) NO_2 plume rotated with its wind direction around the source (star) to an upwind-downwind pattern. Grey boxes centered around black points indicate the extent of the spatial integration of NO_2 columns to obtain the NO_2 line density. Values of cardinal points are noted in black. (right) Corresponding line densities (points) representing the downwind evolution of NO_2 as function of the distance to Riyadh's city centre, and the corresponding fit according to the exponentially modified Gaussian function (dashed line).

330 The phenomena under study here take place in the planetary boundary layer (PBL), which in this region has
 331 a midday height of about 2 km (Filioglou et al., 2020 [64]). TROPOMI observations only provide information on the total
 332 NO_2 content of the tropospheric column, without providing information on the vertical distribution of concentrations.
 333 Extracting emissions from concentrations therefore requires a selection on the height at which wind, temperature and
 334 OH data are taken. Lama et al., 2020 [19] and Lorente et al., 2019 [16] conducted similar studies using the boundary
 335 layer average wind, while Beirle et al., 2019 [15] chose a vertical level of about 450 m above ground. Because vertical
 336 transport of NO_x , which is emitted mainly from combustion engines and industrial stacks, is generally minor compared
 337 to horizontal transport, NO_x is confined to the first few hundred metres above ground level. Using PBL-averaged data
 338 poses a problem of consistency as wind, temperature and OH concentration values significantly vary within the PBL.
 339 As a consequence, we compare the CAMS-induced lifetime τ and the fit-induced lifetime τ_{fit} using the parameters (\mathbf{w} ,
 340 $[\text{OH}]$ and T) at two different vertical levels: a medium level \mathcal{A} at 925 hPa (about 770 m above ground level), and
 341 a bottom level \mathcal{B} at 987.5 hPa (about 210 m). These levels are interpolated from four and two ECMWF or CAMS
 342 consecutive pressure levels respectively (1000-850 hPa for level \mathcal{A} and 1000-975 hPa for level level \mathcal{B}). Most mask cells
 343 having an altitude between 0 and 150 m, the corresponding pressure variations are small (up to ~ 16 hPa), which
 344 allows us to neglect the effects of topography on the position of pressure levels. Figure 4 sums up the selection method
 345 for the comparison of lifetimes.

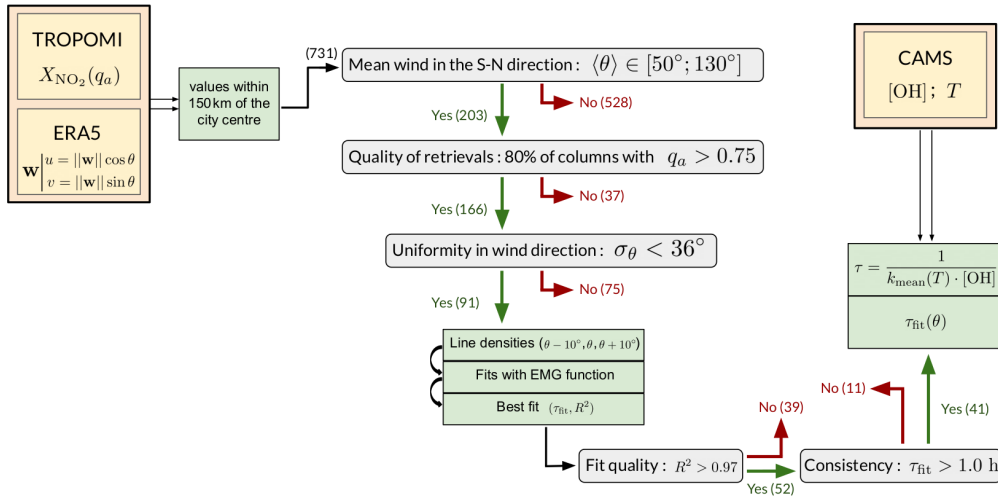


Figure 4: Selection method for NO_2 patterns over Riyadh. Datasets (yellow-orange) are used to calculate the quantities (light green) that are submitted to different tests (grey). 731 patterns are progressively conserved (green arrows) or rejected (red arrows). At each stage, the number of conserved or rejected patterns are noted within brackets (the value is only given for calculations performed at level \mathcal{B}). This selection process compares the lifetimes estimated by the EMG function fitting with TROPOMI line density profiles to the lifetimes calculated according to Equation (2) with CAMS data.

346 3.4 Calculation of anthropogenic NO_x emissions and comparison with inventories

347 We calculate NO_x emissions on the entire domain from NO_2 production by using CAMS NO and NO_2 concentrations.
 348 These are not intended to replace TROPOMI observations; they are used to apply the concentration ratio
 349 $[\text{NO}_x]/[\text{NO}_2] = ([\text{NO}] + [\text{NO}_2])/[\text{NO}_2]$ to account for the conversion of NO_2 to NO and vice versa. As diurnal NO
 350 concentrations in urban areas generally range from 10 to 150 ppb (Khoder, 2008 [65]), the characteristic stabilization
 351 time of this ratio never exceeds a few minutes (Graedel et al., 1976 [66]; Seinfeld and Pandis, 2006 [67]). This time
 352 being lower than the order of magnitude of the inter-mesh transport time (about 30 min considering the resolution
 353 used and the mean wind module in the region), we can reasonably neglect the effect of the stabilization time of the
 354 conversion factor on the total composition of the emissions and treat each cell of the grid independently from its
 355 neighbours. Beirle et al., 2019 [15] found an annual average of 1.32 for this conversion factor, but CAMS data shows
 356 small deviations from this value over Egyptian urban areas. We therefore calculate NO_x emissions for each cell of the
 357 domain as follows:

$$e_{\text{NO}_x} = \frac{[\text{NO}_x]}{[\text{NO}_2]} e_{\text{NO}_2} \quad (6)$$

358 For convenience, quantities $\frac{[\text{NO}_x]}{[\text{NO}_2]}\text{div}(\Omega_{\text{NO}_2}\mathbf{w})$ and $\frac{[\text{NO}_x]}{[\text{NO}_2]}\Omega_{\text{NO}_2}/\tau$ represent the respective contributions of the trans-
 359 port and the sink terms to total NO_x emissions. We finally obtain the emissions related to human activity E_{NO_x} by
 360 removing the arithmetic mean value of NO_x emissions above background cells from total emissions:

$$E_{\text{NO}_x} = e_{\text{NO}_x} - \frac{1}{n_b} \sum_{i=1}^{n_b} e_{\text{NO}_x,i} \quad (7)$$

361 These removed emissions are linked to the NO_2 background estimated by TROPOMI, and do not correspond to
 362 anthropogenic emissions. They provide the value of what must be subtracted from the estimates to obtain emissions
 363 related to human activity. Such a removal assumes that other processes involved in NO_x budgets lead to similar
 364 emissions inside and outside the mask, which is not evident, as the majority of background cells are located in the
 365 desert or the ocean while the majority of mask cells are located near the Nile River. However, as the processes involved
 366 in natural NO_x sources lead to emissions much smaller than anthropogenic emissions in polluted areas, we neglect
 367 this difference in the following calculations. An alternative would be to calculate an average concentration for the
 368 background cells and subtract the corresponding value from the column densities before calculating the emissions.
 369 This would pose further reliability problems: for instance, very high NO_2 concentrations could appear outside the
 370 mask due to wind transport (an example is shown on Figure 1). They would lead to an overestimation of the NO_2
 371 background and thus to an underestimation of the anthropogenic emissions.

372 Neglecting the part of the country that lies outside the domain, total emissions from the anthropogenic activity of
 373 Egypt can then be obtained by integrating E_{NO_x} on the whole domain. For robust statistics, these derived emissions
 374 can be averaged monthly, enabling a month-by-month comparison with bottom-up inventories. The linearity of the
 375 averaging processes ensures the interchangeability of temporal and spatial averages. A monthly average is relevant
 376 because it aggregates enough data to limit the high inter-day variability due to changing wind patterns or differences
 377 between week days and week-ends. In addition, it enables the study of monthly NO_x emission profiles which reflect
 378 changes in human activities throughout the year due to temperature changes, economic constraints and cultural norms.

379 4 Results and discussion

380 4.1 Line densities and NO_2 lifetime

381 We compare the results of the TROPOMI line densities fits for Riyadh to the lifetime calculated by Equation (2) using
 382 CAMS OH data. The two years of TROPOMI observations (from November 2018 to November 2020) provide a wide
 383 variety of profiles. For level \mathcal{B} , Figure 4 also provides the number of samples that are being kept at each stage of the
 384 process. Of the 731 observations available, 203 have a wind direction in the cone with a north-south orientation with
 385 an aperture of 40° (i.e. between 340° and 20° or between 160° and 200°). Of the remaining observations, 166 occurred
 386 with a sufficiently clear sky to be retained. The criterion of weak variability for the wind direction brings to 91
 387 the number of observations that are kept by the method. On these 91 observations, the line density profiles are calculated
 388 and the fits applied. According to Equation (5), the lifetime is calculated using the mean wind module around the
 389 point source. The two lifetimes are calculated with the parameters taken at the medium level \mathcal{A} or at the top level
 390 \mathcal{B} . Of the 91 fits obtained, 51 are of high quality (correlation coefficient between fit function and line density profile
 391 greater than 0.97) for level \mathcal{A} and 52 for level \mathcal{B} . 39 of these fits lead to a lifetime τ_{fit} greater than 1.0 h for level \mathcal{A}
 392 and 41 for level level \mathcal{B} . All remaining samples correspond to atmospheric conditions with moderate to fast winds,
 393 with a module ranging between 2 and 11 m/s (with an average of 5.9 m/s) for level \mathcal{A} and between 3 and 8 m/s (with
 394 an average of 5.4 m/s) for level \mathcal{B} . These lifetimes are compared to the corresponding lifetimes obtained from CAMS
 395 data in Figure 5, which is divided into seasons for a more convenient comparison. The use of level \mathcal{A} leads to notable
 396 underestimations of the NO_2 lifetime in autumn compared to the lifetime calculated with the fitting method. This
 397 same level leads to lifetime overestimations in winter. This trend is not found with the use of level \mathcal{B} , which leads to
 398 a better reproduction of the lifetimes calculated with the fitting method for the available seasons. Figure 5 shows a
 399 linear regression between the two calculated lifetimes. The results are scattered, with a correlation coefficient higher
 400 for level \mathcal{B} (0.408) than for level \mathcal{A} (0.220). When the intercept of the regression line is forced to zero, the resulting
 401 slope is closer to 1 for level \mathcal{B} (0.998) than for level \mathcal{A} (1.071).

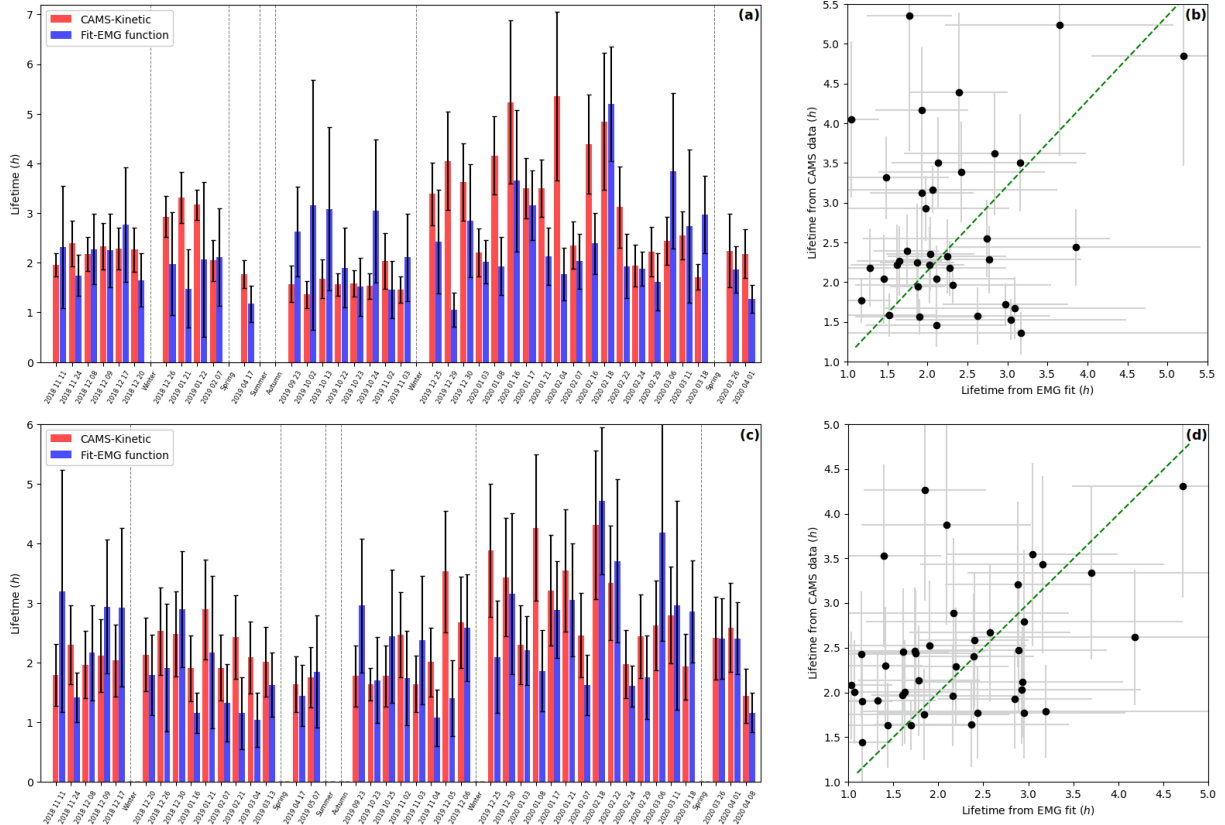


Figure 5: (left) Comparison between CAMS-derived NO_2 lifetimes and lifetimes from NO_2 line density fittings with EMG function above Riyadh city centre, for level \mathcal{A} (a) and \mathcal{B} (c). The samples presented correspond to patterns in clear-sky conditions for which the mean wind is in the north-south direction with a low variance, and for which the correlation between line density profile and fit gives a correlation coefficient of more than 0.97 and a lifetime of more than 1.0 h. NO_2 patterns do not have these conditions during the summers of 2019 and 2020. Dashed lines separate the groups of observations by season. (right) Comparison between the two calculated lifetimes for level \mathcal{A} (b) and \mathcal{B} (d). A linear regression with an intercept forced to be zero is displayed with a green dashed line.

Level \mathcal{B} is therefore the one that leads to the best match between the lifetime calculated with Equation (2) and the lifetime calculated from line densities. The results that are presented in the following sections (except for Section 4.3) are therefore results of calculations performed with parameters (\mathbf{w} , $[\text{OH}]$, T and $[\text{NO}_x]/[\text{NO}_2]$) estimated at level \mathcal{B} . Nevertheless, it should be noted that no summer observations were included in the comparison. The main reason for this is the wind direction: of the 188 summer days observed, 178 have a mean wind direction outside the north-south cone over central Riyadh. On the remaining ten days (one for summer 2019 and nine for summer 2020), the ERA5 wind direction is too variable for the fit to be considered relevant, or the fit results in a correlation coefficient below 0.97. It is not clear how correctly the NO_2 lifetime would be calculated during both summer periods by Equation (2). With OH concentrations being the main driver of this lifetime, we cannot assess the relevance of the representation of OH concentrations by CAMS data during summer days in the study.

4.2 Mapping of Egypt's NO_x emissions

The top-down emission model is then applied to the Egyptian domain with CAMS OH concentration and temperature fields for lifetime calculations. For each cell, NO_x emissions are calculated according to Equation (6), resulting in a mapping of Egypt's emissions. The obtained values are averaged monthly from November 2018 to November 2020. Figure 6 shows a composition of the emissions map with the transport term and the sink term for the months of January and July 2019. The corresponding anthropogenic emissions, calculated according to Equation (7), are added. The Nile appears on transport term maps: the divergence calculation complies with what is expected from a line of emitters, i.e. a clear separation of zones of positive divergence from zones of negative divergence with a separation line corresponding to the course of the river. The fact that areas of negative and positive divergence are respectively located to the east and the west of the river is the result of the zonal component of the wind being positive most of the time. Some point sources like Cairo, Alexandria, Asyut or Aswan are easily identifiable. The sink term, directly proportional to the TROPOMI column densities, also highlights these cities. However, unlike the transport term,

424 which has a similar spatial pattern from month to month, the sink term is clearly stronger in summer than in winter.
 425 This is mainly due to a higher lifetime in winter than in summer (4.94 h on average in January 2019 and 2.62 h in July
 426 2019) while the average TROPOMI NO_2 concentrations are slightly higher during winter (1.071×10^{15} molecules. cm^{-2}
 427 for January 2019 and 0.899×10^{15} molecules. cm^{-2} for July 2019). Over the whole domain, the mean transport term
 428 varies throughout the studied period between -0.014×10^{15} molecules. $\text{cm}^{-2}.\text{h}^{-1}$ (December 2019) and 0.015×10^{15}
 429 molecules. $\text{cm}^{-2}.\text{h}^{-1}$ (May 2020). Thus, it hardly contributes to the NO_x emission budget, the mean chemical sink
 430 term alone varying between 0.223×10^{15} molecules. $\text{cm}^{-2}.\text{h}^{-1}$ (December 2019) and 0.534×10^{15} molecules. $\text{cm}^{-2}.\text{h}^{-1}$
 431 (September 2020).

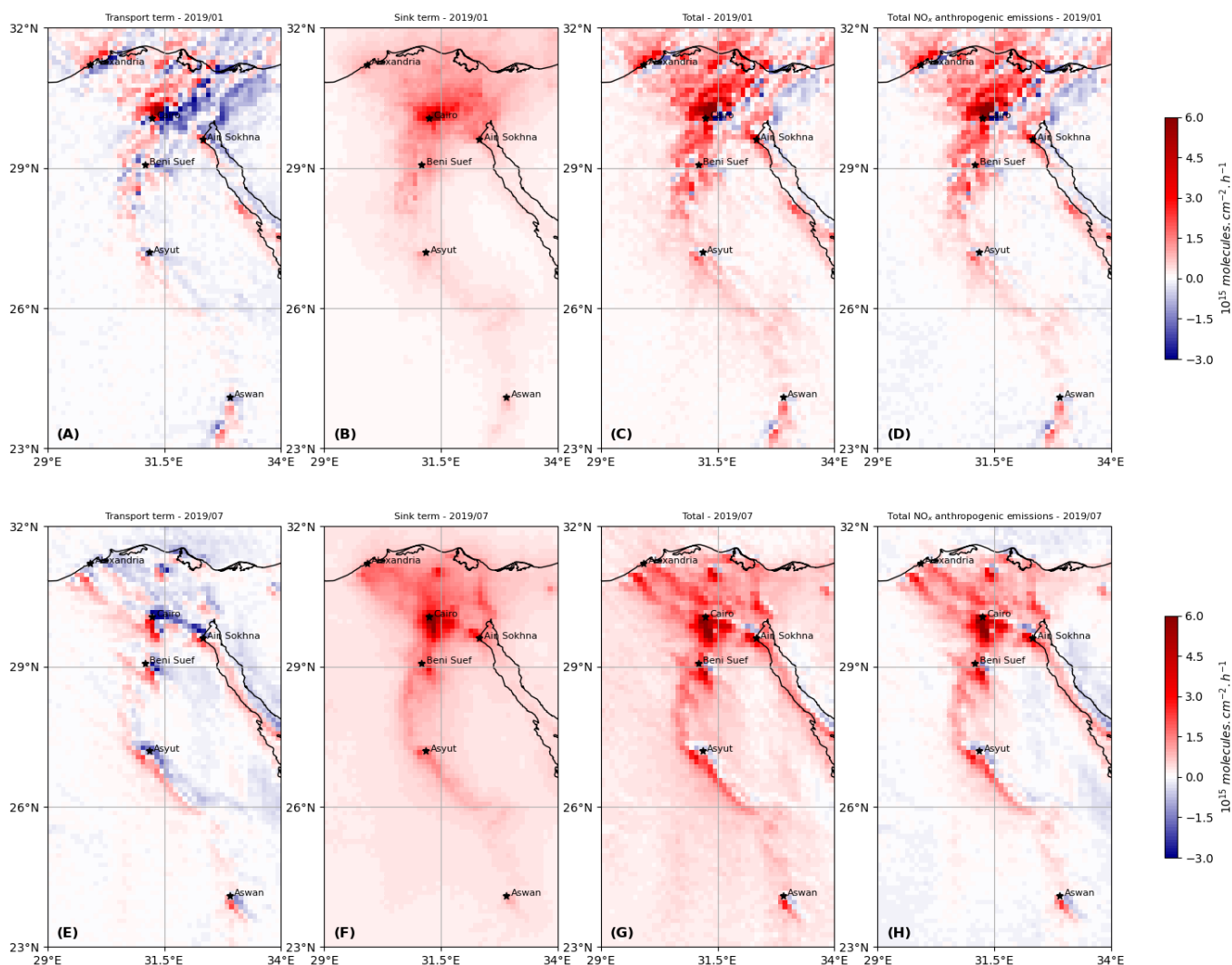


Figure 6: NO_x emissions above most of Egypt's territory: (top) transport term (A), sink term (B), resulting surface emissions (C), and the corresponding anthropogenic emissions after non-anthropogenic background removal (D) for January 2019. (bottom) transport term (E), sink term (F), resulting surface emissions (G), and the corresponding anthropogenic emissions after non-anthropogenic background removal (H) for July 2019.

432 Several cities in the country appear as the main emitters of the country, such as Cairo, Alexandria, Beni Suef, Asyut
 433 or Aswan. The industrial area of Ain-Sokhna, located southwest of Suez, also appears as a main emitter. Table 1
 434 compares the monthly values for the sink term and the absolute value of the transport term above five major cities
 435 of the country, with populations ranging from 200,000 to 20 million inhabitants, as well as Ain-Sokhna's area. The
 436 mean values for TROPOMI column densities are also provided. According to the results, the capital city of Cairo is
 437 by far the largest emitter in the country, largely due to its large population, resulting in high traffic emissions, but also
 438 to its intensive industrial activity. Alexandria, the country's second largest city, is not necessarily the second largest
 439 emitter, as its emissions are comparable to those of smaller cities such as Beni Suef or Asyut. However, the three
 440 cities concentrate a large amount of industrial activity: Alexandria hosts several oil and gas power plants and a small

441 number of cement factories, while Beni Suef is close to several oil and gas power plants and hosts several flaring sites.
 442 Similarly, the city centre of Asyut is close to three oil and gas-fired power plants and a cement factory. This seems
 443 to indicate that industrial activity might be the main cause of NO_x emissions differences between these cities, before
 444 population size. This explains why NO_x emissions from these three cities are comparable to those of the industrial
 445 area of Ain Sokhna, which includes several cement facilities, iron smelters and oil and gas plants. It might also explain
 446 why Aswan, which has a population that is comparable to Beni Suef or Asyut, but which does not have any major
 447 industrial site, has slightly lower emissions than the two other cities. An additional analysis of the differences between
 448 Asyut and Aswan is provided in Section 4.6. Finally, the Gulf of Suez displays relatively large emissions, which might
 449 be attributed to the shipping sector, the region being a major gateway for international trade. Because it also hosts
 450 several flaring sites, these emissions might also be due to the oil and gas extraction activity.

| City | Population density (habitants per square kilometer) | Jan. 2019 | | | Jul. 2019 | | |
|------------|--|--|--|-------|--|--|-------|
| | | Ω_{NO_2} | Transport | Sink | Ω_{NO_2} | Transport | Sink |
| | | ($\mathcal{M}_{\text{NO}_2} \cdot \text{cm}^{-2}$) | ($\mathcal{M}_{\text{NO}_x} \cdot \text{cm}^{-2} \cdot \text{h}^{-1}$) | | ($\mathcal{M}_{\text{NO}_2} \cdot \text{cm}^{-2}$) | ($\mathcal{M}_{\text{NO}_x} \cdot \text{cm}^{-2} \cdot \text{h}^{-1}$) | |
| Cairo | 18,064 | 9.415 | 2.903 | 3.684 | 5.618 | 2.022 | 4.879 |
| Alexandria | 9,133 | 3.034 | 1.179 | 0.975 | 1.674 | 0.410 | 1.421 |
| Asyut | 1,644 | 1.708 | 0.679 | 0.718 | 2.137 | 1.236 | 1.520 |
| Aswan | 319 | 0.976 | 0.182 | 0.473 | 0.871 | 0.308 | 0.523 |
| Beni Suef | 2,056 | 2.950 | 0.548 | 1.080 | 2.321 | 0.428 | 1.591 |
| Ain Sokhna | 5 | 3.133 | 1.256 | 1.115 | 2.561 | 1.346 | 1.757 |

Table 1: Comparison between the transport term and the sink term above different cities in Egypt, as well as the industrial region of Ain Sokhna located 45 km southwest of Suez for January and July 2019. TROPOMI vertical NO₂ columns, NO_x emissions and population densities correspond to average values within 18 km from the city centre. Unit \mathcal{M} stands for a quantity of 10¹⁵ molecules (NO₂ or NO_x).

451 Although these cities and areas can be described as high-emission sites, the term responsible for these emissions differ
 452 from one site to the other. Figure 7 shows the contribution of the transport term (taken in absolute value) to total
 453 emissions for January and July 2019. Because wind fields are relatively homogeneous along the Nile on spatial scales
 454 of less than 100 km, NO₂ concentration gradients perceived by TROPOMI in the region mainly contribute to the
 455 increase of the transport term which can reach similar values as the sink term. However, it is never significantly higher
 456 than the sink term: due to a spread of the emissions over large urban areas, the behaviour of these cities is therefore
 457 different from that of a point source for which the transport term would be very high (Beirle et al., 2021 [68]).

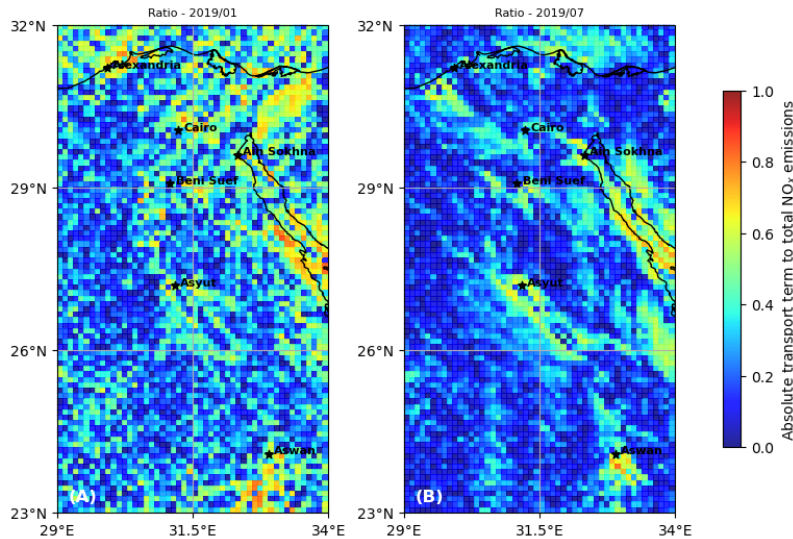


Figure 7: Share of the absolute value of the transport term in the sum of the sink term and the absolute value of the transport term above most of Egypt's territory, indicating the local importance of the transport term in NO_x emissions above mask cells. The average of this ratio is shown for January 2019 (A) and July 2019 (B).

458 Desert areas such as the Libyan Desert, the Eastern Desert and the Sinai region, (located respectively to the west,
 459 east and northeast of the Nile) show a very low value for the transport term compared to the sink term, due to the

460 homogeneity of both the wind field and the detected NO_2 concentrations in these areas. In the case of the Gulf of
 461 Suez, the transport term can be 1 to 2 times higher than the sink term, which varies between 0.4 and 1.2×10^{15}
 462 $\text{molecules.cm}^{-2}.\text{h}^{-1}$. Those values are slightly higher than the average emissions above background cells areas due to
 463 the sink term (about $0.2 - 0.6 \times 10^{15} \text{ molecules.cm}^{-2}.\text{h}^{-1}$), but remain quite low compared to the emissions in large
 464 cities. This relative predominance of the transport term is explained by a visible gradient of the TROPOMI NO_2
 465 column densities. The region thus acts as a very thin line of emitters. Nevertheless, this predominance might also
 466 be partly due to a poor representation of the wind field. The low resolution of ERA-5 (about 26 km in this region,
 467 which is the same order of magnitude as the width of the channel) may misrepresent the wind near the coast, creating
 468 artificial gradients.

469 4.3 Vertical analysis

470 Here we investigate the influence of the choice of the vertical level in the representation of the model parameters.
 471 This influence is of considerable importance, as NO_x sources in urban areas can be located at different altitudes. For
 472 instance, emissions from the road sector from tailpipes are located at ground level, whereas NO_x from power plants
 473 and industrial facilities can be emitted from stacks, which are usually located between 50 and 300 m above the ground.
 474 Section 4.1 results showed that level \mathcal{B} was more appropriate for the representation of the NO_2 lifetime. This level is
 475 therefore chosen as a reference for the comparison. We study the effect of a transition from level \mathcal{B} to level \mathcal{A} for each
 476 of the 3 parameters involved in the representation of the sink term, i.e. temperature T , hydroxyl radical concentration
 477 $[\text{OH}]$ and concentration ratio $[\text{NO}_x]/[\text{NO}_2]$. The results for the averages over mask cells and background cells are
 478 given for the months of January, April, July and October 2019 in Table 2. As the wind field is only involved in the
 479 transport term whose spatial integration nearly leads to zero, the influence of this parameter is not studied.

| | | Sink term ($10^{15} \text{ molecules.cm}^{-2}.\text{h}^{-1}$) | | | | | | | |
|---|---------------------------------------|---|-------------------|-------------------|-------------------|-------------------|-------------------|-------------------|-------------------|
| level \mathcal{B} (987.5 hPa) | level \mathcal{A} (925 hPa) | Jan. 19 (MASK) | Jan. 19 (BKGD) | Apr. 19 (MASK) | Apr. 19 (BKGD) | Jul. 19 (MASK) | Jul. 19 (BKGD) | Oct. 19 (MASK) | Oct. 19 (BKGD) |
| $T, [\text{OH}], \frac{[\text{NO}_x]}{[\text{NO}_2]}$ | - | 0.859 | 0.253 | 1.072 | 0.345 | 1.125 | 0.376 | 0.932 | 0.277 |
| $[\text{OH}], \frac{[\text{NO}_x]}{[\text{NO}_2]}$ | T | 0.899 (+4.7%) | 0.264 (+4.2%) | 1.127 (+5.2%) | 0.361 (+4.6%) | 1.185 (+5.3%) | 0.394 (+4.9%) | 0.887 (+4.8%) | 0.264 (+4.5%) |
| $T, \frac{[\text{NO}_x]}{[\text{NO}_2]}$ | $[\text{OH}]$ | 0.769 (-10.5%) | 0.219 (-13.6%) | 1.013 (-5.5%) | 0.324 (-6.0%) | 1.129 (+0.4%) | 0.375 (-0.3%) | 0.853 (-8.5%) | 0.251 (-9.5%) |
| $T, [\text{OH}]$ | $\frac{[\text{NO}_x]}{[\text{NO}_2]}$ | 0.872 (+1.6%) | 0.257 (+1.4%) | 1.094 (+2.1%) | 0.352 (+2.0%) | 1.143 (+1.6%) | 0.383 (+1.9%) | 0.904 (+3.1%) | 0.271 (+2.2%) |

Table 2: Analysis of the effect of a vertical change in the parameters used to estimate the sink term in NO_x emissions: temperature, hydroxyl radical concentration, and $\text{NO}_x:\text{NO}_2$ concentration ratio. The comparison is conducted between the estimated quantities for level \mathcal{B} and level \mathcal{A} . The comparison is conducted for mask cells (MASK) and background cells (BKGD) for four months of the year 2019. Values within brackets represent the variation from the base case for which all quantities are estimated at level \mathcal{B} .

480 The transition to level \mathcal{A} generally results in a decrease in temperature, leading to an increase in the reaction rate k_{mean}
 481 and thus an increase in the emissions from the sink term. This transition has only a small influence on the total NO_x
 482 emission estimates, with mask and background cells emissions increasing by 4 to 6%. The influence of OH goes in the
 483 opposite direction: its concentration decreases with altitude, weakening the sink term. This weakening is particularly
 484 visible during winter months, for which the emissions are lower by up to 14%. In summer however, the effect is
 485 hardly noticeable. Finally, the influence of the $\text{NO}_x:\text{NO}_2$ ratio is negligible on the NO_x emission estimates. Thus,
 486 the transition to level \mathcal{A} results in an increase in the sink term of 1 to 4%, due to a decrease in both concentrations
 487 of NO and NO_2 with respect to the vertical but with a greater decrease for NO_2 . This vertical study confirms the
 488 crucial importance of the OH concentration for the accurate representation of NO_x emissions. It appears here as
 489 an important driver of the sink term, which is much more sensitive to vertical differences than temperature or the
 490 $\text{NO}_x:\text{NO}_2$ concentration ratio.

491 4.4 Weekly cycle

492 In Egypt, the official rest day is Friday, and the economic activity of the country is *a priori* lower during this day than
 493 during the other days of the week. We therefore try to characterise this feature, by evaluating the weekly cycle of
 494 NO_x emissions. We use the TROPOMI-inferred emissions to obtain averages per day of the week. We use the quality
 495 assurance q_a of TROPOMI retrievals to ignore the days for which more than 20% of the domain has low-quality data
 496 (this happens 43 times in 2018/2019 and 28 times in 2019/2020). Such a filtering avoids accounting for the days when

497 a large part of the urban and industrial areas are covered by clouds. However, it misses situations where small clouds
 498 are localised over large emitters, in which case the corresponding emissions are under-estimated. Figure 8 shows the
 499 resulting daily emissions for the period November 2018 - November 2019 and November 2019 - November 2020. NO_x
 500 emissions are expressed in mass terms as NO. A Friday minimum is observed, defining a weekly cycle. This trend is
 501 also observed for mean NO_2 column densities, for which no intra-weekly variation is observed. Over the 2018-2019
 502 period, Fridays have average emissions of 0.811 ± 0.408 kt, which is lower than average emissions for the rest of the
 503 week, which reach 0.997 ± 0.533 kt. A similar trend is observed in 2019-2020, for which the average for Fridays is
 504 0.704 ± 0.357 kt and the average for other days is 0.921 ± 0.449 kt. The difference in emissions between the two periods
 505 is due to smaller emissions in December 2019, January 2020 and February 2020 that are discussed in Section 4.5. On
 506 average, Friday emissions correspond to a ratio of 0.83:7 (i.e. a value of 0.83 after normalisation on the seven days of
 507 the week) for the entire domain. This result is consistent with the values obtained by Stavrakou et al., 2020 [69], who
 508 used TROPOMI data and another emission model to calculate a ratio of 0.71:7 for Cairo and 0.89:7 for Alexandria in
 509 2017.

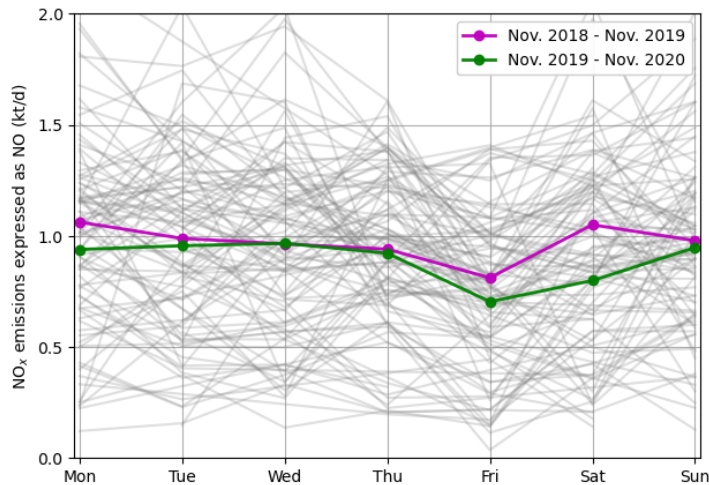


Figure 8: Weekly profiles of anthropogenic NO_x emissions for Egypt using TROPOMI observations in 2018-2019 (purple line) and 2019-2020 (green line). Thin grey lines represent individual weeks. Days for which less than 80% of the domain counts low quality observations ($q_a < 0.75$) are not represented.

510 4.5 Impacts of lockdown during COVID-19

511 The ongoing global outbreak of COVID-19 forced many countries around the world to implement unprecedented
 512 public health responses, including travel restrictions, quarantines, curfews and lockdowns. Such measures have helped
 513 to counter the spread of the virus and have, meanwhile, caused high reductions in global demand for fossil fuels (IEA,
 514 2020 [70]). They also led to a fall in the levels of NO_2 and other air pollutants across the globe (Venter et al., 2020
 515 [71]; Bauwens et al., 2020 [72]; Gkatzelis et al., 2021 [73]). To prevent the spread of COVID-19, Egyptian authorities
 516 ordered a partial lockdown from March 15th till June 30th 2020, closing all public areas (e.g. sport centres, nightclubs,
 517 restaurants and cafes) and suspending religious activities in all mosques and churches throughout the country. They
 518 also implemented more drastic measures such as a full lockdown during Easter (April 20th) and Eid (May 23rd to
 519 May 25th), before lifting some restrictions on June 1st (Hale et al., 2021 [74]). In addition to the effect of containment
 520 on the activity of the country, the global decline in consumption led to a drop in the production of certain industrial
 521 products.

522 Several studies have estimated the impact of these events on the air pollution levels in the urban centres of the
 523 country : from in-situ measurements, El-Sheekh et al., 2021 [75] estimated that NO_2 concentrations had dropped by
 524 25.9% in Alexandria's city centre after the start of the lockdown on March 13th, while El-Magd et al., 2020 [76] used
 525 OMI retrievals to estimate a 45.5% reduction of NO_2 concentrations for the entire country during the spring compared
 526 to 2018 and 2019 average values. However, due to a changing lifetime of NO_2 , reductions in the concentrations of NO_2
 527 might not be entirely due to a decrease in NO_x emissions, which leads us to focus on the variation of NO_x emissions
 528 during this singular period. Using our top-down emission model, reductions in total NO_x emissions of 20.1%, 11.8%
 529 and 13.5% are observed for the months of March, April and May 2020 compared to the equivalent months in 2019.
 530 This drop of emissions in 2020 compared to 2019 calculated by the model also correspond to a decrease in observed

531 NO₂ columns. No significant changes in OH concentrations seem to appear: on average, from 2019 to 2020, CAMS
 532 near-real-time data shows a decrease of 5.5% for OH concentration over the mask cells for the period March/April/May,
 533 while TROPOMI retrievals above mask cells show a decrease in NO₂ column densities of 21.6% over the same period.
 534 However, these effects observed for the months of March, April and May 2020 are not repeated in June 2020, for
 535 which emissions show an increase of 15.8% compared to June 2019. This rise is largely the result of an increase in the
 536 difference between average estimates inside and outside the mask. Indeed, emissions within the mask in June 2020 are
 537 higher than those of June 2019, due to an increase in TROPOMI concentrations above mask cells (+7.7%) while the
 538 NO₂ lifetime is almost unchanged (+3.3%). Emissions outside the mask varies in the opposite direction: a decrease
 539 in TROPOMI background concentrations (-5.4%) is observed while NO₂ lifetime increases strongly (+16.0%). This
 540 increase in June emissions seems to indicate that the lift on restrictions allowed a catch-up of the economic activity
 541 which was sufficiently strong to generate higher emissions in 2020 than in 2019.

542 4.6 Annual cycle and comparison to inventories

543 Here, we attempt to compare our TROPOMI-derived NO_x emissions to emissions from CAMS-GLOB-ANT_v4.2 and
 544 EDGARv5.0 inventories. Figure 9 shows the total anthropogenic NO_x emissions over the mask cells from November
 545 2018 to November 2020, calculated according to Equation (7). As indicated in Section 3.2, the emissions, calculated
 546 at 13:30 local time, are representative of the average daily consumption in Egypt. The total calculated for each month
 547 therefore corresponds to the NO_x production by human activities in the country. After aggregating the different
 548 sectors of activity, CAMS and EDGAR inventories directly provide the anthropogenic NO_x emissions over the same
 549 domain. All NO_x emissions are expressed in mass terms as NO. We note that the EDGAR inventory does not cover
 550 the period 2018-2020 (the last available year of the inventory is 2015). On Figure 9, EDGAR emissions corresponding
 551 to the period between November 2013 and November 2015 are displayed, i.e. the preceding 5 years compared to
 552 TROPOMI-derived emissions and CAMS estimates.

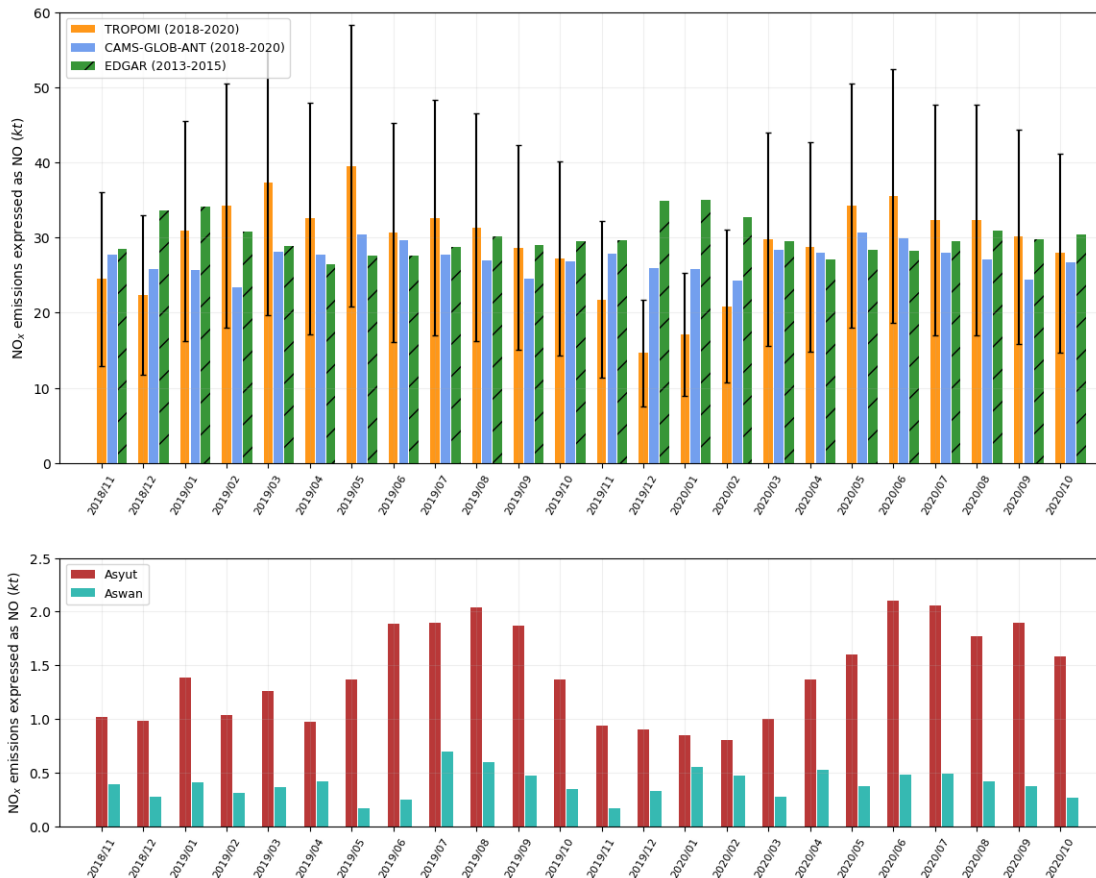


Figure 9: (top) Comparison of TROPOMI-derived anthropogenic NO_x emissions in Egypt (light blue), with the corresponding emissions from EDGAR (green with stripes) and CAMS (yellow) inventories. EDGAR data is shown for comparison purposes and covers the years 2013-2015. (bottom) TROPOMI-derived anthropogenic NO_x emissions for the cities of Asyut (dark red) and Aswan (light blue). The corresponding domains are displayed on Figure 1.

553 TROPOMI-derived emissions are higher than the CAMS inventory estimates. The top-down model estimates total
554 emissions of 697.6 kt over the 24 months, which is 45.9 kt higher than CAMS for the same period (651.6 kt). This
555 difference is primarily localized in the first 12 months, for which TROPOMI-inferred emissions are always higher
556 than the inventories and show higher values in summer than during the rest of the year. The next 12 months show
557 similar emissions in summer but much lower values in winter. In particular, the difference is significant in December
558 2019 and January 2020 (respectively 56.5% and 66.5% of CAMS levels). These emissions also contrast with other
559 winter emissions, with a total of 31.7 kt for 2019-12/2020-01 against 53.3 kt for 2018-12/2019-01 and 57.7 kt for
560 2020-12/2021-01. In the computations, this drop for winter 2019/2020 is mainly due to a relatively low value of
561 the OH concentration which reaches 4.61×10^6 molecules.cm⁻³ on average for December 2019 and January 2020,
562 with 4.29×10^6 molecules.cm⁻³ above mask cells and 4.69×10^6 molecules.cm⁻³ over background cells. They were
563 respectively 5.29 , 5.74 and 5.18×10^6 molecules.cm⁻³ for the previous year (2018-12/2019-01) and 5.11 , 4.90 and 5.16
564 $\times 10^6$ molecules.cm⁻³ for the subsequent year (2020-12/2021-01). A decrease in tropospheric columns (-18.5% for
565 mask cells and -7.6% for background cells compared to winter 2018/2019) also contributes to this drop. The accuracy
566 of the inferred emissions for winter 2019/2020 can therefore be questioned.

567 At first sight, the annual variability of TROPOMI-inferred emissions, which describes a one-year cycle with higher
568 emissions in summer, seems to be correlated with power emissions which dominate the use of fossil fuels in Egypt
569 (Abdallah et al., 2020 [77]). These power emissions are due to the country’s residential electricity consumption (Attia
570 et al., 2012 [59]; Elharidi et al., 2013 [78]; Nassief, 2014 [79]). They also meet the needs of industry. Summer peaks
571 in electricity consumption are mostly driven by temperature, as illustrated by the increasing sales of air conditioning
572 and ventilation systems for several decades (Wahba et al., 2018 [80]). The use of air conditioning in cars, which
573 requires an additional amount of fuel, could also contribute to the increase of NO_x emissions in summer. To support
574 this hypothesis, we use our model on two smaller domains centered around the two cities of Asyut and Aswan. The
575 corresponding domains are displayed on Figure 1. Both cities have similar demographic features, with populations of
576 about 467,000 and 315,000 inhabitants in 2021 and human densities of about 3,000 and 1,600 inhabitants per square
577 kilometer respectively. However, their industrial features largely differ. There is no large fossil fuel-fired power plant
578 in Aswan, where most of the electricity is produced by a hydroelectric dam, whereas Asyut counts three oil and gas
579 power plants of various capacities (90, 650 and 1500 MW) in its urban area. Both cities have a cement plant, but
580 the one in Asyut has a larger production capacity (5.7 Mt/yr in Asyut, 0.8 Mt/yr in Aswan). Our model is used
581 following the same procedure as for the main domain. The background removal is done at the scale of the country.
582 A seasonal cycle appears for Asyut, with a minimum for winter months and a maximum for summer months. This
583 cycle seems slightly shifted from the one observed for the entire country, for which May emissions are as important
584 as those of summer months. We also note that the decrease in emissions for winter 2019/2020 is less marked than for
585 the emissions of the whole country, and of a similar value to the previous winter. This suggests that national NO_x
586 emissions are indeed lower during winter, but that the values obtained for winter 2019/2020 are particularly low. We
587 also find that the seasonality of the emissions is more pronounced for the Asyut domain than for the country as a
588 whole. The case of Aswan is different. Emissions within the corresponding domain are significantly lower than for
589 Asyut. The signal-to-noise ratio being higher, it is difficult to characterise an annual cycle, but the results do not seem
590 to indicate low emissions in winter and high emissions in summer. This identification of a seasonal cycle identical to
591 that of the entire country for a city with several power plants, and the absence of such a cycle in a city without any,
592 strengthens the hypothesis that the power sector plays a major role in Egyptian NO_x emissions.

593 We note that some features of the industrial activities in the country might be counteracting this trend. For some
594 sectors such as cement or steel, production is lower in summer, due to the physical wear experienced by workers due
595 to heat, but also due to certain periods of leave. Given the importance of industrial activities in the production of
596 NO_x shown in Section 4.2, this aspect cannot be neglected. The transport sector could also counteract the observed
597 trend: although the use of air conditioning in cars increase NO_x emissions of the sector, the observed mean traffic
598 in the country is higher between November and February and lower between June and August, especially in Cairo
599 which gathers most of the population. In the absence of additional data, it therefore seems difficult to conclude on the
600 amplitude of the seasonal cycle produced by our top-down model. This caution is all the more necessary as CAMS
601 and EDGAR show seasonal cycles for NO_x emissions, with different dynamics than those displayed by TROPOMI
602 emissions: while the EDGAR inventory predicts a maximum of emissions in December or January and a minimum
603 in April, the CAMS inventory shows two local maxima each year in May and November and two local minima in
604 February and September. The amplitude of the corresponding cycles is much lower in those inventories, representing
605 14.2% of the average value for emissions estimates for EDGAR and 12.4% for CAMS. Those values must be compared
606 to the amplitude displayed by TROPOMI-inferred emissions, for which the maximum/minimum ratio is about 1.8 if
607 winter 2019/2020 is excluded, and 2.7 if it is included.

608 4.7 Uncertainties and assessments of results

609 The estimation of NO_x emissions is based on the use of several quantities with varying uncertainties. The error bars
610 shown in Figures 5 and 9 are thus calculated from uncertainty statistics whose references are presented in this section.
611 Since these references do not specify the exact nature of these statistics, we assume they correspond to standard
612 deviations. The uncertainty of tropospheric NO_2 columns under polluted conditions is dominated by the sensitivity
613 of satellite observations to lower tropospheric air masses, expressed by the tropospheric air-mass factor (AMF). The
614 column relative uncertainty due to the AMF is of the order of 30% (Boersma et al., 2004 [43]). S-5P validation
615 activities indicate that TROPOMI tropospheric NO_2 columns are systematically biased low by about 30%-50% over
616 cities (Compernolle et al., 2018 [81]), which is most likely related to the *a priori* profiles used within the operational
617 retrieval that do not reflect well the NO_2 peak close to ground. For the Middle East region, the impact of the *a priori*
618 profile is less critical, as surface albedo is generally high and cloud fractions are generally low. Thus, we expect no
619 such bias, and consider a relative uncertainty of 30% for the tropospheric column. Other uncertainties must be taken
620 into account: the transition from NO_2 TROPOMI columns to NO_x emissions requires parameters which appear in
621 Equation (2) and Equation (3). For wind module, uncertainties are generally of about 1 m/s for components taken
622 at precise altitudes (Coburn et al., 2019 [82]; Beirle et al., 2019 [15]). Here, we assume an uncertainty of 3 m/s for
623 both zonal and meridional wind components. For [OH], the analysis of different methods conducted by Huijnen et
624 al., 2019 [83] showed smaller differences for low latitudes than for extratropics, but still significant. We thus take a
625 relative uncertainty of 30% for OH concentration. For the reaction rate k_{mean} , the value of the corresponding relative
626 uncertainty has been estimated by Burkholder et al., 2020 [30]. Finally, we use the sensitivity tests performed in
627 Section 4.3 to assess the uncertainty associated with the choice of the vertical level. The cumulative effects on the
628 final emissions of the three parameters studied, in particular the OH concentration, lead to a relative uncertainty that
629 varies from month to month between 7 and 18%. The propagation of these different uncertainties on the monthly
630 estimates of NO_x emissions in Egypt leads to an expanded uncertainty between 47 and 51%. For lifetimes calculated
631 with the EMG function fitting, the corresponding expanded uncertainty ranges between 18% and 79%.

632 We acknowledge the fact that our treatment of NO_x is simplified. Many minor sinks highlighted in Section 3.1
633 are not taken into account. In particular, anthropogenic VOC emissions, which remove NO_x from the atmosphere,
634 compete with the oxidation by OH for the representation of NO_x loss. These emissions are difficult to estimate and
635 the corresponding sink is complex to model. Taking this reaction into account would *a priori* lead to a strengthening
636 of the sink term and thus to an increase of the NO_x emissions estimates. Other assumptions in the model are also
637 simplifications. For instance, obtaining anthropogenic emissions by subtracting the average emissions over background
638 cells assumes that the non-anthropogenic sources of NO_2 are similar inside and outside the mask, which is not true,
639 since a large part of the mask cells correspond to croplands. For these cells, soil emissions may play a non-negligible
640 role in the natural NO_2 budget. As a consequence, mean background emissions that are removed from NO_x emissions
641 estimates above mask cells might be under-estimated. Finally, the reliability of the data used can be questioned. The
642 representation of the wind is crucial to avoid creating artificial patterns in the transport term. The OH concentration,
643 which is proportional to the intensity of the sink term, is also important. We have shown that OH concentrations
644 are partially responsible for an important drop in NO_x emissions in the winter of 2019/2020 that may be unrealistic.
645 Because this decrease is largely due to variations in OH concentrations provided by CAMS, whose reliability has
646 been evaluated for Riyadh, then the transposability hypothesis between Riyadh and Egypt may be subject to further
647 discussion.

648 5 Conclusions

649 In this study, we investigated the potential of a top-down model of NO_x emissions based on TROPOMI retrievals at
650 high resolution over Egypt. The model is based on the study of a transport term and a sink term that requires different
651 parameters to be calculated. Among those parameters, the concentration in OH, involved in the calculation of the NO_2
652 mixed lifetime, is of fundamental importance. The comparison between NO_2 lifetimes derived from OH concentrations
653 and NO_2 lifetimes derived from EMG function fittings of line density profiles shows that the OH concentration provided
654 by CAMS is reasonably reliable for the country. Parameters are therefore taken in the first 200 m of the planetary
655 boundary layer, because it is where OH shows the best consistency. However, the vertical sensitivity linked to this
656 parameters remains high. Results illustrate the importance of the transport term at local scale, which is of the same
657 order of magnitude as the sink term above large cities and industrial facilities; it ceases to be relevant only at the
658 scale of the whole country. The top-down model is able to characterise declines in human activities due to restrictions
659 during the COVID-19 pandemic or to Friday rest. It also estimates higher emissions during summer. These high
660 emissions may be interpreted by a higher consumption of electricity driven by air-conditioning during hot days, but it

661 remains unclear whether this pattern clearly reproduces changes in human activity, in particular because the emission
662 inventories show different seasonalities. These inventories also differ in the amount of total emissions: the average
663 value for TROPOMI-derived NO_x emissions is 7.0% higher than CAMS estimates. This discrepancy could be resolved
664 by comparing the results of the model and inventory estimates to industrial production or electricity consumption
665 data at the scale of countries or regions.

666 This study demonstrates the potential of TROPOMI data for evaluating NO_x emissions in the Middle East region.
667 More generally, it demonstrates the importance of the contribution of independent observation systems to overcome
668 the weaknesses of emission inventories, provided that the local chemistry is well understood and modelled. The
669 development of similar applications for different species is likely to allow better monitoring of global anthropogenic
670 emissions, therefore helping companies and countries to report their emissions of air pollutants and greenhouse gases
671 as part of their strategies and obligations to tackle air pollution issues and climate change.

672 **Data availability.**

673 TROPOMI product: <http://www.tropomi.eu/data-products/data-access>
674 CAMS NRT: <https://ads.atmosphere.copernicus.eu/cdsapp!/dataset/cams-global-atmospheric-composition-forecasts>
675 ERA5 reanalysis: <https://cds.climate.copernicus.eu/cdsapp!/dataset/reanalysis-era5-pressure-levels-monthly-means>
676 Global Rural-Urban Mapping Project (GRUMP): <https://sedac.ciesin.columbia.edu/data/collection/grump-v1>
677 Oil and gas power plants: <http://globalenergyobservatory.org/>
678 Industrial facilities: <https://www.industryabout.com>
679 Flaring sites: https://eogdata.mines.edu/download_global_flare.html
680 CAMS-GLOB-ANT_v4.2: <https://permalink.aeris-data.fr/CAMS-GLOB-ANT>
681 EDGARv5.0: https://edgar.jrc.ec.europa.eu/dataset_ap50

682 **Competing interests.** The authors declare that they have no conflict of interest.

683 **Acknowledgements.** The authors would like to thank Steven J. Davis (University of California, Irvine) and Dan
684 Tong (Tsinghua University) for their contribution to the construction of our emitters database.

685 **Financial support.** This study has been funded by the European Union’s Horizon 2020 research and innovation
686 programme under grant agreement N° 856612 (EMME-CARE).

687 **References**

- 688 [1] A. Baklanov, L. T. Molina, and M. Gauss, “Megacities, air quality and climate,” *Atmospheric Environment*,
689 vol. 126, pp. 235–249, 2016.
- 690 [2] L. Tang, X. Xue, M. Jia, H. Jing, T. Wang, R. Zhen, M. Huang, J. Tian, J. Guo, L. Li, *et al.*, “Iron and steel
691 industry emissions and contribution to the air quality in China,” *Atmospheric Environment*, vol. 237, p. 117668,
692 2020.
- 693 [3] H. C. Kim, C. Bae, M. Bae, O. Kim, B.-U. Kim, C. Yoo, J. Park, J. Choi, J.-b. Lee, B. Lefer, *et al.*, “Space-Borne
694 monitoring of NO_x emissions from cement kilns in South Korea,” *Atmosphere*, vol. 11, no. 8, p. 881, 2020.
- 695 [4] A. Singh and M. Agrawal, “Acid rain and its ecological consequences,” *Journal of Environmental Biology*, vol. 29,
696 no. 1, p. 15, 2007.
- 697 [5] U. EPA, “Integrated science assessment for oxides of nitrogen—health criteria,” *US Environmental Protection*
698 *Agency, Washington, DC [Google Scholar]*, 2016.
- 699 [6] M. Crippa, G. Janssens-Maenhout, F. Dentener, D. Guizzardi, K. Sindelarova, M. Muntean, R. Van Dingenen,
700 and C. Granier, “Forty years of improvements in European air quality: regional policy-industry interactions with
701 global impacts,” *Atmospheric Chemistry and Physics*, vol. 16, no. 6, pp. 3825–3841, 2016.

- 702 [7] A. El-Magd, N. Zanaty, E. M. Ali, H. Irie, A. I. Abdelkader, *et al.*, “Investigation of aerosol climatology, optical
703 characteristics and variability over Egypt based on satellite observations and in-situ measurements,” *Atmosphere*,
704 vol. 11, no. 7, p. 714, 2020.
- 705 [8] UNEP (United Nations Environment Programme), “Air quality policies in Egypt,” 2015.
- 706 [9] B. Xue and W. Ren, “China’s uncertain CO₂ emissions,” *Nature Climate Change*, vol. 2, no. 11, pp. 762–762,
707 2012.
- 708 [10] C. Leue, M. Wenig, T. Wagner, O. Klimm, U. Platt, and B. Jähne, “Quantitative analysis of NO_x emissions from
709 global ozone Monitoring Experiment satellite image sequences,” *Journal of Geophysical Research: Atmospheres*,
710 vol. 106, no. D6, pp. 5493–5505, 2001.
- 711 [11] R. V. Martin, D. J. Jacob, K. Chance, T. P. Kurosu, P. I. Palmer, and M. J. Evans, “Global inventory of nitrogen
712 oxide emissions constrained by space-based observations of NO₂ columns,” *Journal of Geophysical Research:*
713 *Atmospheres*, vol. 108, no. D17, 2003.
- 714 [12] B. Mijling and R. Van Der A, “Using daily satellite observations to estimate emissions of short-lived air pollutants
715 on a mesoscopic scale,” *Journal of Geophysical Research: Atmospheres*, vol. 117, no. D17, 2012.
- 716 [13] B. de Foy, Z. Lu, D. G. Streets, L. N. Lamsal, and B. N. Duncan, “Estimates of power plant NO_x emissions and
717 lifetimes from OMI NO₂ satellite retrievals,” *Atmospheric Environment*, vol. 116, pp. 1–11, 2015.
- 718 [14] D. L. Goldberg, Z. Lu, D. G. Streets, B. de Foy, D. Griffin, C. A. McLinden, L. N. Lamsal, N. A. Krotkov, and
719 H. Eskes, “Enhanced Capabilities of TROPOMI NO₂: Estimating NO_x from North American Cities and Power
720 Plants,” *Environmental science & technology*, vol. 53, no. 21, pp. 12594–12601, 2019.
- 721 [15] S. Beirle, C. Borger, S. Dörner, A. Li, Z. Hu, F. Liu, Y. Wang, and T. Wagner, “Pinpointing nitrogen oxide
722 emissions from space,” *Science advances*, vol. 5, no. 11, p. eaax9800, 2019.
- 723 [16] A. Lorente, K. Boersma, H. Eskes, J. Veefkind, J. Van Geffen, M. De Zeeuw, H. D. van der Gon, S. Beirle, and
724 M. Krol, “Quantification of nitrogen oxides emissions from build-up of pollution over Paris with TROPOMI,”
725 *Scientific reports*, vol. 9, no. 1, pp. 1–10, 2019.
- 726 [17] K. Lange, A. Richter, and J. P. Burrows, “Variability of nitrogen oxide emission fluxes and lifetimes estimated
727 from Sentinel-5P TROPOMI observations,” *Atmospheric Chemistry and Physics Discussions*, pp. 1–32, 2021.
- 728 [18] J. Veefkind, I. Aben, K. McMullan, H. Förster, J. De Vries, G. Otter, J. Claas, H. Eskes, J. De Haan, Q. Kleipool,
729 *et al.*, “TROPOMI on the ESA Sentinel-5 Precursor: A GMES mission for global observations of the atmospheric
730 composition for climate, air quality and ozone layer applications,” *Remote sensing of environment*, vol. 120,
731 pp. 70–83, 2012.
- 732 [19] S. Lama, S. Houweling, K. F. Boersma, H. Eskes, I. Aben, H. A. Denier van der Gon, M. C. Krol, H. Dol-
733 man, T. Borsdorff, and A. Lorente, “Quantifying burning efficiency in megacities using the NO₂/CO ratio from
734 the Tropospheric Monitoring Instrument (TROPOMI),” *Atmospheric Chemistry and Physics*, vol. 20, no. 17,
735 pp. 10295–10310, 2020.
- 736 [20] H. Eskes, K. Eichmann, J. Lambert, D. Loyola, J. Veefkind, A. Dehn, and C. Zehner, “S5P Mission Performance
737 Centre Nitrogen Dioxide [L2_NO2] readme,” *Royal Netherlands Meteorological Institute (KNMI) De Bilt, the*
738 *Netherlands, version*, vol. 1, no. 00, 2019.
- 739 [21] H. Hersbach, B. Bell, P. Berrisford, S. Hirahara, A. Horányi, J. Muñoz-Sabater, J. Nicolas, C. Peubey, R. Radu,
740 D. Schepers, *et al.*, “The ERA5 global reanalysis,” *Quarterly Journal of the Royal Meteorological Society*, vol. 146,
741 no. 730, pp. 1999–2049, 2020.
- 742 [22] V. Huijnen, H. Eskes, A. Wagner, M. Schulz, Y. Christophe, M. Ramonet, S. Basart, A. Benedict-
743 tow, A.-M. Blechschmidt, S. Chabrilat, *et al.*, “Validation report of the CAMS near-real-time global at-
744 mospheric composition service: System evolution and performance statistics. Status up to 1 June 2016;
745 https://pure.mpg.de/rest/items/item_2441827/component/file_2441834/content,” 2016.
- 746 [23] J. H. Seinfeld, “Urban air pollution: state of the science,” *Science*, vol. 243, no. 4892, pp. 745–752, 1989.

- 747 [24] J. A. Logan, M. J. Prather, S. C. Wofsy, and M. B. McElroy, "Tropospheric chemistry: a global perspective,"
748 *Journal of Geophysical Research: Oceans*, vol. 86, no. C8, pp. 7210–7254, 1981.
- 749 [25] H. Levy, "Normal atmosphere: Large radical and formaldehyde concentrations predicted," *Science*, vol. 173,
750 no. 3992, pp. 141–143, 1971.
- 751 [26] L. Valin, A. Russell, R. Hudman, and R. Cohen, "Effects of model resolution on the interpretation of satellite
752 NO₂ observations," *Atmospheric Chemistry and Physics*, vol. 11, no. 22, pp. 11647–11655, 2011.
- 753 [27] J. Lelieveld, S. Gromov, A. Pozzer, and D. Taraborrelli, "Global tropospheric hydroxyl distribution, budget and
754 reactivity," *Atmospheric Chemistry and Physics*, vol. 16, no. 19, pp. 12477–12493, 2016.
- 755 [28] M. Li, E. Karu, C. Brenninkmeijer, H. Fischer, J. Lelieveld, and J. Williams, "Tropospheric OH and stratospheric
756 OH and Cl concentrations determined from CH₄, CH₃Cl, and SF₆ measurements," *NPJ Climate and Atmospheric
757 Science*, vol. 1, no. 1, pp. 1–7, 2018.
- 758 [29] G. M. Wolfe, J. M. Nicely, J. M. S. Clair, T. F. Hanisco, J. Liao, L. D. Oman, W. B. Brune, D. Miller, A. Thames,
759 G. G. Abad, *et al.*, "Mapping hydroxyl variability throughout the global remote troposphere via synthesis of
760 airborne and satellite formaldehyde observations," *Proceedings of the National Academy of Sciences*, vol. 116,
761 no. 23, pp. 11171–11180, 2019.
- 762 [30] J. Burkholder, S. Sander, J. Abbatt, J. Barker, C. Cappa, J. Crounse, T. Dibble, R. Huie, C. Kolb, M. Kurylo,
763 *et al.*, "Chemical kinetics and photochemical data for use in atmospheric studies; evaluation number 19," tech.
764 rep., Pasadena, CA: Jet Propulsion Laboratory, National Aeronautics and Space . . . , 2020.
- 765 [31] J. Yienger and H. Levy, "Empirical model of global soil-biogenic NO_x emissions," *Journal of Geophysical Research:
766 Atmospheres*, vol. 100, no. D6, pp. 11447–11464, 1995.
- 767 [32] J. J. Hoelzemann, M. G. Schultz, G. P. Brasseur, C. Granier, and M. Simon, "Global wildland fire emission model
768 (GWEM): Evaluating the use of global area burnt satellite data," *Journal of Geophysical Research: Atmospheres*,
769 vol. 109, no. D14, 2004.
- 770 [33] D. H. Ehhalt, F. Rohrer, and A. Wahner, "Sources and distribution of NO_x in the upper troposphere at northern
771 mid-latitudes," *Journal of Geophysical Research: Atmospheres*, vol. 97, no. D4, pp. 3725–3738, 1992.
- 772 [34] L. Jaeglé, L. Steinberger, R. V. Martin, and K. Chance, "Global partitioning of NO_x sources using satellite
773 observations: Relative roles of fossil fuel combustion, biomass burning and soil emissions," *Faraday discussions*,
774 vol. 130, pp. 407–423, 2005.
- 775 [35] J.-F. Müller and T. Stavrou, "Inversion of CO and NO_x emissions using the adjoint of the images model,"
776 *Atmospheric Chemistry and Physics*, vol. 5, no. 5, pp. 1157–1186, 2005.
- 777 [36] J.-T. Lin, "Satellite constraint for emissions of nitrogen oxides from anthropogenic, lightning and soil sources over
778 East China on a high-resolution grid," *Atmospheric Chemistry and Physics*, vol. 12, no. 6, pp. 2881–2898, 2012.
- 779 [37] CIESIN, "CIESIN. Global Rural-Urban Mapping Project, Version 1 (GRUMPv1). Center for International Earth
780 Science Information Network - CIESIN - Columbia University, International Food Policy Research Institute -
781 IFPRI, The World Bank, and Centro Internacional de Agricultura Tropical - CIAT. 2011, Palisades, NY: NASA
782 Socioeconomic Data and Applications Center (SEDAC)," 2019.
- 783 [38] C. D. Elvidge, M. Zhizhin, K. Baugh, F.-C. Hsu, and T. Ghosh, "Methods for global survey of natural gas flaring
784 from visible infrared imaging radiometer suite data," *Energies*, vol. 9, no. 1, p. 14, 2016.
- 785 [39] M. Crippa, D. Guizzardi, M. Muntean, E. Schaaf, E. Solazzo, F. Monforti-Ferrario, J. Olivier, and E. Vignati,
786 "Fossil CO₂ emissions of all world countries," *Luxembourg: European Commission*, pp. 1–244, 2020.
- 787 [40] C. Granier, S. Darras, H. D. van der Gon, D. Jana, N. Elguindi, G. Bo, G. Michael, G. Marc, J.-P. Jalkanen,
788 J. Kuenen, *et al.*, *The Copernicus atmosphere monitoring service global and regional emissions (April 2019
789 version)*. PhD thesis, Copernicus Atmosphere Monitoring Service, 2019.
- 790 [41] R. M. Hoesly, S. J. Smith, L. Feng, Z. Klimont, G. Janssens-Maenhout, T. Pitkanen, J. J. Seibert, L. Vu, R. J.
791 Andres, R. M. Bolt, *et al.*, "Historical (1750–2014) anthropogenic emissions of reactive gases and aerosols from
792 the community emissions data system (CEDS)," *Geoscientific Model Development*, vol. 11, no. 1, pp. 369–408,
793 2018.

- 794 [42] G. Janssens-Maenhout, M. Crippa, D. Guizzardi, M. Muntean, E. Schaaf, F. Dentener, P. Bergamaschi,
795 V. Pagliari, J. G. Olivier, J. A. Peters, *et al.*, “Edgar v4. 3.2 global atlas of the three major greenhouse gas
796 emissions for the period 1970–2012,” *Earth System Science Data*, vol. 11, no. 3, pp. 959–1002, 2019.
- 797 [43] K. Boersma, H. Eskes, and E. Brinksma, “Error analysis for tropospheric NO₂ retrieval from space,” *Journal of*
798 *Geophysical Research: Atmospheres*, vol. 109, no. D4, 2004.
- 799 [44] A. Lorente, K. Folkert Boersma, H. Yu, S. Dörner, A. Hilboll, A. Richter, M. Liu, L. N. Lamsal, M. Barkley,
800 I. D. Smedt, *et al.*, “Structural uncertainty in air mass factor calculation for NO₂ and HCHO satellite retrievals,”
801 *Atmospheric Measurement Techniques*, vol. 10, no. 3, pp. 759–782, 2017.
- 802 [45] S. Sander, R. Friedl, J. Abbatt, J. Barker, J. Burkholder, D. Golden, C. Kolb, M. Kurylo, G. Moortgat, P. Wine,
803 *et al.*, “Chemical kinetics and photochemical data for use in atmospheric studies, jpl publication 10-6,” *Evaluation*,
804 no. 17, 2011.
- 805 [46] B. A. Nault, C. Garland, P. J. Wooldridge, W. H. Brune, P. Campuzano-Jost, J. D. Crouse, D. A. Day, J. Dibb,
806 S. R. Hall, L. G. Huey, *et al.*, “Observational constraints on the oxidation of NO_x in the upper troposphere,” *The*
807 *Journal of Physical Chemistry A*, vol. 120, no. 9, pp. 1468–1478, 2016.
- 808 [47] T. Stavroukou, J.-F. Müller, K. Boersma, R. Van Der A, J. Kurokawa, T. Ohara, and Q. Zhang, “Key chemical
809 NO_x sink uncertainties and how they influence top-down emissions of nitrogen oxides,” *Atmospheric Chemistry*
810 *and Physics*, vol. 13, no. 17, pp. 9057–9082, 2013.
- 811 [48] H. Fang, F. Baret, S. Plummer, and G. Schaepman-Strub, “An overview of global leaf area index (LAI): Methods,
812 products, validation, and applications,” *Reviews of Geophysics*, vol. 57, no. 3, pp. 739–799, 2019.
- 813 [49] E. R. Delaria, B. K. Place, A. X. Liu, and R. C. Cohen, “Laboratory measurements of stomatal NO₂ deposition
814 to native california trees and the role of forests in the NO_x cycle,” *Atmospheric Chemistry and Physics*, vol. 20,
815 no. 22, pp. 14023–14041, 2020.
- 816 [50] N. Sobanski, J. Thieser, J. Schuladen, C. Sauvage, W. Song, J. Williams, J. Lelieveld, and J. N. Crowley, “Day
817 and night-time formation of organic nitrates at a forested mountain site in south-west germany,” *Atmospheric*
818 *Chemistry and Physics*, vol. 17, no. 6, pp. 4115–4130, 2017.
- 819 [51] A. Guenther, T. Karl, P. Harley, C. Wiedinmyer, P. I. Palmer, and C. Geron, “Estimates of global terrestrial
820 isoprene emissions using megan (model of emissions of gases and aerosols from nature),” *Atmospheric Chemistry*
821 *and Physics*, vol. 6, no. 11, pp. 3181–3210, 2006.
- 822 [52] P. S. Romer Present, A. Zare, and R. C. Cohen, “The changing role of organic nitrates in the removal and
823 transport of NO_x,” *Atmospheric Chemistry and Physics*, vol. 20, no. 1, pp. 267–279, 2020.
- 824 [53] N. Butkovskaya, A. Kukui, N. Pouvesle, and G. Le Bras, “Formation of nitric acid in the gas-phase HO₂+NO
825 reaction: Effects of temperature and water vapor,” *The Journal of Physical Chemistry A*, vol. 109, no. 29,
826 pp. 6509–6520, 2005.
- 827 [54] N. Butkovskaya, M.-T. Rayez, J.-C. Rayez, A. Kukui, and G. Le Bras, “Water vapor effect on the HNO₃ yield in
828 the HO₂+NO reaction: experimental and theoretical evidence,” *The Journal of Physical Chemistry A*, vol. 113,
829 no. 42, pp. 11327–11342, 2009.
- 830 [55] N. Friedrich, P. Eger, J. Shenolikar, N. Sobanski, J. Schuladen, D. Dienhart, B. Hottmann, I. Tadic, H. Fischer,
831 M. Martinez, *et al.*, “Reactive nitrogen around the arabian peninsula and in the mediterranean sea during the
832 2017 AQABA ship campaign,” *Atmospheric Chemistry and Physics*, vol. 21, no. 10, pp. 7473–7498, 2021.
- 833 [56] W. Moxim, H. Levy, and P. Kasibhatla, “Simulated global tropospheric PAN: Its transport and impact on NO_x,”
834 *Journal of Geophysical Research: Atmospheres*, vol. 101, no. D7, pp. 12621–12638, 1996.
- 835 [57] E. Fischer, D. J. Jacob, R. M. Yantosca, M. P. Sulprizio, D. Millet, J. Mao, F. Paulot, H. Singh, A. Roiger,
836 L. Ries, *et al.*, “Atmospheric peroxyacetyl nitrate (PAN): a global budget and source attribution,” *Atmospheric*
837 *Chemistry and Physics*, vol. 14, no. 5, pp. 2679–2698, 2014.
- 838 [58] C. A. Longfellow, A. Ravishankara, and D. R. Hanson, “Reactive uptake on hydrocarbon soot: Focus on NO₂,”
839 *Journal of Geophysical Research: Atmospheres*, vol. 104, no. D11, pp. 13833–13840, 1999.

- 840 [59] S. Attia, A. Evrard, and E. Gratia, "Development of benchmark models for the Egyptian residential buildings
841 sector," *Applied Energy*, vol. 94, pp. 270–284, 2012.
- 842 [60] EEHC, "Egyptian Electricity Holding Company annual report 2019/2020," 2021.
- 843 [61] F. Rohrer and H. Berresheim, "Strong correlation between levels of tropospheric hydroxyl radicals and solar
844 ultraviolet radiation," *Nature*, vol. 442, no. 7099, pp. 184–187, 2006.
- 845 [62] S. Beirle, K. F. Boersma, U. Platt, M. G. Lawrence, and T. Wagner, "Megacity emissions and lifetimes of nitrogen
846 oxides probed from space," *Science*, vol. 333, no. 6050, pp. 1737–1739, 2011.
- 847 [63] L. Valin, A. Russell, and R. Cohen, "Variations of OH radical in an urban plume inferred from NO₂ column
848 measurements," *Geophysical Research Letters*, vol. 40, no. 9, pp. 1856–1860, 2013.
- 849 [64] M. Filioglou, E. Giannakaki, J. Backman, J. Kesti, A. Hirsikko, R. Engelmann, E. O'Connor, J. T. Leskinen,
850 X. Shang, H. Korhonen, *et al.*, "Optical and geometrical aerosol particle properties over the United Arab Emirates,"
851 *Atmospheric Chemistry and Physics*, vol. 20, no. 14, pp. 8909–8922, 2020.
- 852 [65] M. Khoder, "Diurnal, seasonal and weekdays-weekends variations of ground level ozone concentrations in an
853 urban area in greater cairo," *Environmental Monitoring and Assessment*, vol. 149, no. 1, pp. 349–362, 2009.
- 854 [66] T. Graedel, L. Farrow, and T. Weber, "Kinetic studies of the photochemistry of the urban troposphere," *Atmo-
855 spheric Environment (1967)*, vol. 10, no. 12, pp. 1095–1116, 1976.
- 856 [67] J. H. Seinfeld and S. N. Pandis, "Atmospheric chemistry and physics from air pollution to climate change," 2006.
- 857 [68] S. Beirle, C. Borger, S. Dörner, H. Eskes, V. Kumar, A. de Laat, and T. Wagner, "Catalog of NO_x emissions
858 from point sources as derived from the divergence of the NO₂ flux for TROPOMI," *Earth System Science Data*,
859 vol. 13, no. 6, pp. 2995–3012, 2021.
- 860 [69] T. Stavrou, J.-F. Müller, M. Bauwens, K. Boersma, and J. van Geffen, "Satellite evidence for changes in the
861 NO₂ weekly cycle over large cities," *Scientific reports*, vol. 10, no. 1, pp. 1–9, 2020.
- 862 [70] U. IEA, "Global energy review 2020," *Ukraine.[Online]* <https://www.iea.org/countries/ukraine> [Accessed: 2020-
863 09-10], 2020.
- 864 [71] Z. S. Venter, K. Aunan, S. Chowdhury, and J. Lelieveld, "COVID-19 lockdowns cause global air pollution declines,"
865 *Proceedings of the National Academy of Sciences*, vol. 117, no. 32, pp. 18984–18990, 2020.
- 866 [72] M. Bauwens, S. Compernelle, T. Stavrou, J.-F. Müller, J. Van Gent, H. Eskes, P. F. Levelt, R. van der A,
867 J. Veeffkind, J. Vlietinck, *et al.*, "Impact of coronavirus outbreak on NO₂ pollution assessed using TROPOMI and
868 OMI observations," *Geophysical Research Letters*, vol. 47, no. 11, p. e2020GL087978, 2020.
- 869 [73] G. I. Gkatzelis, J. B. Gilman, S. S. Brown, H. Eskes, A. R. Gomes, A. C. Lange, B. C. McDonald, J. Peischl,
870 A. Petzold, C. R. Thompson, *et al.*, "The global impacts of COVID-19 lockdowns on urban air pollution: a critical
871 review and recommendations," *Elementa: Science of the Anthropocene*, vol. 9, no. 1, 2021.
- 872 [74] T. Hale, N. Angrist, R. Goldszmidt, B. Kira, A. Petherick, T. Phillips, S. Webster, E. Cameron-Blake, L. Hallas,
873 S. Majumdar, *et al.*, "A global panel database of pandemic policies (oxford covid-19 government response tracker),"
874 *Nature Human Behaviour*, vol. 5, no. 4, pp. 529–538, 2021.
- 875 [75] M. M. El-Sheekh and I. A. Hassan, "Lockdowns and reduction of economic activities during the COVID-19
876 pandemic improved air quality in Alexandria, Egypt," *Environmental Monitoring and Assessment*, vol. 193,
877 no. 1, pp. 1–7, 2021.
- 878 [76] I. Abou El-Magd and N. Zanaty, "Impacts of short-term lockdown during COVID-19 on air quality in Egypt,"
879 *The Egyptian Journal of Remote Sensing and Space Science*, 2020.
- 880 [77] L. Abdallah and T. El-Shennawy, "Evaluation of CO₂ emission from Egypt's future power plants," *Euro-
881 Mediterranean Journal for Environmental Integration*, vol. 5, no. 3, pp. 1–8, 2020.
- 882 [78] A. M. A. H. Elharidi, P. G. Tuohy, and M. Teamah, "Facing the growing problem of the electric power consumption
883 in Egyptian residential building using building performance simulation program," in *Building simulation Cairo
884 2013 conference*, 2013.

- 885 [79] M. M. Nassief, "Evaluation of electricity consumption of a residential flat in egypt," *American Journal of Electrical*
886 *Power and Energy Systems*, vol. 3, no. 2, pp. 7–44, 2014.
- 887 [80] S. M. Wahba, B. A. Kamel, K. M. Nassar, and A. S. Abdelsalam, "Effectiveness of green roofs and green walls on
888 energy consumption and indoor comfort in arid climates," *Civil Engineering Journal*, vol. 4, no. 10, pp. 2284–2295,
889 2018.
- 890 [81] S. Compernelle *et al.*, "S5P MPC VDAF validation web article: Nitrogen dioxide," tech. rep., S5P-MPC-VDAF-
891 WVA-L2_NO2_20180904, 2018.
- 892 [82] J. J. Coburn, "Assessing wind data from reanalyses for the upper midwest," *Journal of Applied Meteorology and*
893 *Climatology*, vol. 58, no. 3, pp. 429–446, 2019.
- 894 [83] V. Huijnen, A. Pozzer, J. Arteta, G. Brasseur, I. Bouarar, S. Chabrillat, Y. Christophe, T. Doumbia, J. Flemming,
895 J. Guth, *et al.*, "Quantifying uncertainties due to chemistry modelling–evaluation of tropospheric composition
896 simulations in the CAMS model (cycle 43r1)," *Geoscientific Model Development*, vol. 12, no. 4, pp. 1725–1752,
897 2019.

898